PRINTED ELECTRONICS FOR MULTI-FUNCTIONAL CARBON FIBER COMPOSITES

MOHAMAD KANNAN IDRIS

A THESIS SUBMITTED TO

THE FACULTY OF GRADUATE STUDIES

IN PARTIAL FULFILLMENT OF THE REQUIREMENTS FOR

THE DEGREE OF

MASTER OF APPLIED SCIENCE

GRADUATE PROGRAM IN

ELECTRICAL ENGINEERING & COMPUTER SCIENCE

YORK UNIVERSITY, TORONTO, ONTARIO

JUNE 2020

ABSTRACT

Extrusion printing is a contactless nozzle-based digital printing method used to print stretchable and flexible circuit elements. Printing electronics on textiles integrates the enhanced functionality of electrical elements with the physical properties of textiles. Extrusion printing on textiles faces challenges that are overcome in this thesis. Extrusion printing is used to print electrical contacts directly on carbon fiber weaves. This can be integrated into structural carbon fiber composites manufactured with traditional methods. by exploiting the thermal and electrical conductivity of carbon fiber, two carbon fiber-based devices are fabricated, a heater and a damage sensor. Unmanned Aerial Vehicles (UAVs) suffer from ice accumulation on wings, and commercial solutions for de-icing are limited. The proposed heater can be integrated into UAV wings for de-icing. Structural Health Monitoring (SHM) aims to detect damage in structures such as cracks and holes using sensors. The proposed damage sensor detects holes in structures for SHM.

ACKNOWLEDGMENTS

First and foremost, I would like to express my gratitude to my mentor and supervisor Dr. Gerd Grau. Without his guidance, motivation, patience and persistent help this thesis would have not been possible. I have learned so many valuable lessons from him about printed electronics, research, writing papers and even career choices, and I am looking forward to learn from him even more.

I would also like to thank Dr. Garrett Melenka. He was my supervisor in the research course of my degree and he continued to offer his help and guidance after that for my research for this thesis. He was always nice and approachable when I needed help and his insights were always valuable. In addition he always made me feel very welcome working in his lab and made sure I had access to all the equipment I needed.

I want to thank Dr. Roger Kempers for graciously agreeing to participate in my oral examination.

I am very grateful for Saifur, Paria and James who supported me and made the long hours in the lab fun along with Mehraneh, Milad, Fahmida, Babak, Amir and Max.

I would like to acknowledge funding support from York University through the Lassonde Innovation Fund (LIF) and we would like to acknowledge CMC Microsystems for the provision of access to Sentaurus.

Finally, I would like to thank my family. My father, Khaldoun is my inspiration. He always pushes me to be a better version of myself. Without his hard work and support I would not have made it anywhere in my life. My mother, Shaden, is my best friend who always made sure that I am happy and healthy. My baby sister, Layla, is always by my side no matter how physically far away from each other we are. They call me every day to check up on me and keep me company. I would like to thank my grandparents, Aref, Ibtihal and Fatat, who always kept me in their prayers and loved me through thick and thin even though I haven’t been able to see them in years. I love you all!

TABLE OF CONTENTS

LIST OF TABLES

LIST OF FIGURES

CHAPTER 1. INTRODUCTION

1.1. Extrusion Printing Electronics on Textiles

Printed electronics is becoming increasingly viable and is considered a key technological enabler for Internet of Things (IoT) due to its potential for mechanical flexibility, low weight, low cost, ecofriendly, on-demand printability and scalability.[1] Multiple printing techniques have been proposed for printed electronics including: inkjet printing, screen printing, gravure printing, and extrusion printing.[2] Inks for such printing techniques can be based on a variety of materials including metal particles or organic materials to print conductors, insulators and semiconductors.

Printing electronics on textiles is interesting because it allows for the integration of the enhanced functionality of electrical elements and the physical properties of textile materials.[3] There are multiple ways to create electronic textiles (e-textiles) including sewing and knitting, weaving, braiding, coating/laminating, chemical treatment and printing.[4] Printing is the most promising method because it is low-cost, scalable and enables the facile customization of designs using digital printing technology. However, textiles are usually fibrous and have high surface roughness thus presenting multiple challenges for the various printing methods.

So far, screen printing has been the most effective and most widely used method to print on textiles. Screen printing is a high-volume mask-based technique. The design of the print is patterned as a mask on a mesh. The ink is spread over the mesh and pushed through it using a squeegee thus creating a pattern on the substrate. This technique is ideal for printing in large scale on a range of materials including textiles, glass, wood and ceramics.[5] Screen printing is commonly used in printed electronics to print interconnects and passive circuit elements.[6] Screen printing creates thick-layer patterns using high-viscosity inks which can overcome the roughness of the textile.[4], [5] Nevertheless, screen printing wastes ink in the process, which, in the case of printing electronics, is not cost-effective due to the expensive materials used in the inks. In addition, it requires a pre-designed mask, which can prove costly if it is required to constantly modify the printing pattern.

Inkjet printing has also been used to print on textiles. Inkjet printing is a non-contact digital additive technique that can deposit ink on various substrates. Droplets are jetted from a nozzle towards the substrate following a layout without using any masks or etching processes, which can make it more cost-effective than screen printing on textiles, especially for low-volume applications.[7] This technique has been used to print various microelectronic devices such as organic thin-film transistors (OTFT), organic light-emitting diodes (OLED) and organic solar cells (OPV).[1], [8] However, the inks used for inkjet have very low viscosities. As a result, to inkjet print on textiles, an interface layer is required to reduce surface roughness and ensure pattern continuity, which is critical for electronics. The interface layer is usually applied to the textile using dip coating, spin coating or even screen printing.[3], [4], [7], [9]

Extrusion printing, also known as dispenser printing, operates by applying pressure to dispense ink through small nozzles (100μm – 250μm) as shown in Figure 1-1. This technique has multiple parameters including ink viscosity, nozzle diameter, nozzle height offset from the substrate, print speed and most importantly, pressure control. Depending on the ink and substrate material, there is an optimal combination of printing parameters. Extrusion printing is commonly used to print metal-based inks, mostly silver, which consist of metal flakes and a polymer binder dissolved in a solvent.[10] Inks for extrusion printing are high viscosity (approximately 10^3 to 10^6 cP) to prevent nozzle leakage.[11] Extrusion printing is considered a digital printing technique that can be used to print flexible and stretchable interconnects and passive circuit elements.[12] Extrusion printing combines the positive attributes of both inkjet and screen printing when used for printing on textiles. It is a contactless nozzle-based method, it is a digital method that does not require a mask, ink is extruded only when needed, and it can print highly viscous inks to create thick-layer patterns which is ideal for printing on textiles.

Extrusion printing faces many challenges when used to print on textiles, foremost is the fact that it requires the nozzle to be very close to the substrate (80-100 μm). When the nozzle is close to the substrate, it can become entangled in the fibers of the textile, thus, either moving and destroying the substrate or damaging the delicate nozzle. So far, no successful extrusion printing attempts on textiles have been reported. In this thesis, a study of extrusion printing electronics on textiles, specifically carbon fiber weaves, is presented.

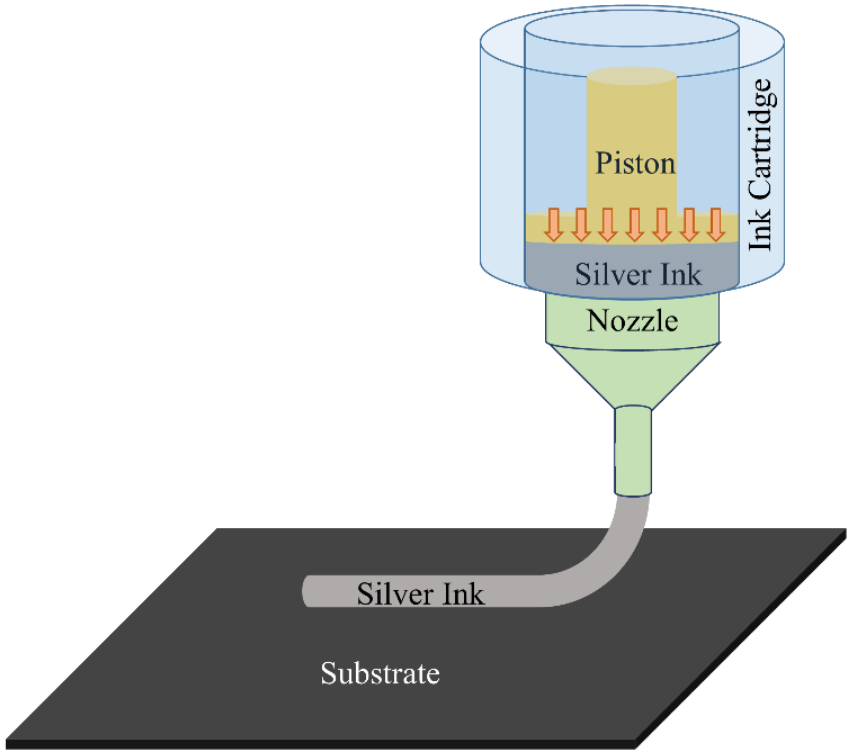

Figure 1-1. Illustration of the extrusion printing process. The piston applies pressure to the ink, which is dragged out of the nozzle as it translates relative to the substrate.

1.2. Carbon Fiber Textile Composites

Carbon fiber is an attractive structural material because of its physical properties such as excellent tensile properties, low density, high strength to weight ratio, high thermal and chemical stability, and good thermal and electrical conductivity.[13] Carbon fiber is commercially available in various forms including single yarns, braids and weaves (e.g. Unidirectional or Twill).

Textile composites are engineered materials that combine the unique physical properties of their multiple components.[14] Most prevalent among textile composites are carbon fiber composites that are commonly used to reinforce structures such as aircraft, vehicles, bridges, and other concrete structures. Carbon fiber textiles are treated with a matrix material (e.g. epoxy, thermoplastics, rubber) to combine the physical properties of carbon fiber and the matrix to create woven carbon fiber composites. The matrix material allows the composite to maintain its structure and shape. Carbon fiber (CF) has a wide variety of desirable properties, including high tensile strength to weight ratio, chemical resistance, and thermal and electrical conductivity, which can be tailored as desired, enabling a wide range of applications. CF composites are currently available in industries such as aerospace, athletics, construction, automotive, defense, marine, and wind energy.[15], [16]

In this thesis, carbon fiber composites are of interest for two applications. First, creating a heating device aimed towards being integrated in carbon fiber wings of unmanned aerial vehicle (UAV) for de-icing. Second, creating a damage sensor aimed towards being integrated in structures for structural health monitoring.

1.3. Carbon Fiber Composites: Integrated Heaters for UAVs

The use of UAVs for information gathering and delivering items to remote areas has notably increased recently.[17] However, like passenger aircraft, ice accretion on wings is problematic for drones.[18] Aircraft icing occurs when water droplets from the air or clouds accumulate and freeze on the surfaces of an aircraft. Ice accretion greatly restricts the performance of aircraft. Ice accretion on the leading edge of a rotorcraft wing blade creates ice shapes that alter the lift, drag and pitching moment characteristics of the wing. In general, the performance of smaller aerial vehicles such as drones, commuter aircraft and small transport aircraft is more affected by icing than that of larger commercial transport aircraft due to their size. Just like rotorcrafts, ice accretion on the wings and tails of the aircraft reduces maximum lift and stall angle of attack, while increasing profile drag.[19] There are several methods for de-icing aircraft wings. De-icing fluids are commonly sprayed on aircraft before takeoff. Such de-icing fluids are usually water-based and include Freeze Point Depressants (FDP), mainly glycol, among other wetting agents and corrosion inhibiting materials.[20] In large commercial aircraft, hot air produced from the engine is pumped through tubes into the inner surface of the wings.[18], [19] In smaller aircraft, electro-thermal systems can be used on surfaces such as intake lips or helicopter rotors.[19] However, commercially available solutions for de-icing of unmanned aerial vehicles are still limited.[21], [22] Carbon fiber composites are being used as tubes connecting the body of a drone to its rotors,[23] or to create the propellers and wings of a UAV.[24] The fact that carbon fibers are electrically and thermally conductive means that they can be directly used as the heating element in an electric heater. This way, an aircraft wing can be heated without the need for a separately applied heater such as a flexible heater on a plastic substrate. This reduces the complexity of integrating a de-icing system into a UAV and reduces cost since the heating element i.e. the structural carbon fiber does not need to be added separately to the system. There are successful reports of creating heaters using graphene, carbon nanotubes and carbon fiber using different methods. One method combines a matrix of carbon fiber pre-impregnated with epoxy (pre-preg) with highly aligned carbon nanotube webs produced by chemical vapor deposition (CVD) and copper foil busses for connections.[25] Another method uses a combination of graphene films and carbon fiber reinforced polymer (CFRP) laminates and copper electrodes.[26] Other methods create de-icing heaters using individual carbon fiber tows either impregnated with epoxy for 3D printing or as wires embedded into concrete.[27]–[29] However, these methods add complex processes or expensive materials to the manufacturing process. They generally do not make use of the same carbon fiber textiles commonly used as a structural material nowadays. Here, we propose to use these textiles as the heating element without major changes to common CFRP manufacturing processes, which requires electrical contacts to be fabricated directly on the carbon fibers.

There have been successful attempts of printing electronics on carbon fiber reinforced polymers (CFRP) using aerosol-jet and inkjet printing to create strain sensors for composites.[30]–[35] However, no successful attempts have been reported to print electronics on dry carbon fiber weaves without an epoxy matrix. Printing directly on dry carbon fibers offers two important advantages. First, the printed silver can make direct contact with the electrically conducting carbon fibers without insulating epoxy in between. This ensures good electrical conduction to the fibers. Second, the silver can be printed on the carbon fiber textile in the flat state without difficulties due to potentially complex 3D geometry. Subsequently, the textile acquires its final shape when it is infused with epoxy e.g. in the form of an aircraft wing.

1.4. Structural Health Monitoring (SHM)

Another application for carbon fiber composites is Structural Health Monitoring (SHM). SHM is the process of identifying deformation and damage in advanced engineering structures by creating a system that combines these structures with an array of multi-purpose sensors.[36] Health monitoring sensors collect data about the different aspects of the mechanical system to report its integrity over time. The damage-sensitive data extracted from the sensors' measurements, along with the statistical analysis of this data, determine the current health of the structure.[37] For long-term use in structures that accumulate damage due to aging and operation environments, SHM is used to assess the ability of the structure to perform its function. SHM is used in many industries, including mechanical, civil, and aerospace, to monitor damage in both products and manufacturing infrastructure, where detecting damage has life-saving and economic impacts.[38], [39] In aerospace, SHM is used for real-time monitoring of aircraft integrity. If damage occurs, it could be detected and reacted to instantly, thus increasing the safety of the craft. Additionally, SHM reduces the time on the ground needed for traditional inspection methods, thus increasing operation time and potentially lowering costs.[40] In civil infrastructures, in addition to providing a continuous assessment of the integrity of bridges and buildings, SHM is used for safety assessments of the structures after disasters and extreme events such as earthquakes, and it provides immediate instructions for planning maintenance and repair.[38], [41]

SHM operates when damage or deformation occurs in the structure. The damage significantly changes a physical property in the system, which alters the measurement response of the system. However, this premise faces various challenges, mainly, that damage is usually localized and may not have a significant effect on the overall measurement response of the system. Another challenge SHM faces is defining the possible damage types that may occur to choose a suitable sensing system. Also, it must be shown that the sensor itself is not damaged before field deployment.[38]

Generally, damage can be defined as an alteration introduced to the structure that affects its performance, such as holes, matrix cracks, fiber breaks, delamination, scratches, bends or corrosion.[37] SHM is achieved using a system that compares the damaged state of the structure to a previous undamaged state.[38] In the past decade, sensing technology has made significant progress, and different types of sensors are becoming commercially available.[41] Ultrasonic SHM sensors transmit and receive waves that follow a waveguide and thus measure with high sensitivity the geometrical changes in the structure. Such sensors suit large stationary structures such as bridges due to their low attenuation over large propagation distances.[42] Piezoelectric wafer active sensors use the Electro-Mechanical Impedance Method to detect damage on structures.[37], [43] These wafers could be permanently mounted on structures such as aging aircraft to monitor fatigue cracks and corrosion.[44], [45] SHM sensors are of interest for integration into textile composites. SHM sensors within textile composites will allow for the capability of in-situ wide-area sensing, and they can be integrated with common manufacturing processes. Integrated SHM sensors create multi-functional textile composites that can monitor and diagnose their health states.[46] Carbon fiber composites are being used as piezo-resistive sensors for SHM embedded in structures such as concrete and glass windmill blades.[47]–[55] These studies embed single fibers or yarns in structures, so the sensing is limited to the direction along the fibers. Another report has used carbon fiber weaves as capacitive electroluminescent sensors for wider area sensing on structure surfaces.[56] CF reinforced polymer (CFRP) pre-impregnated with epoxy resin (prepregs) have been used to monitor strain and surface cracks using resistance measurements during bending tests.[32]–[35] All previous studies were limited to sensing along one direction and had no ability of localizing the damage. Here, the use of carbon fiber textile itself as the sensing element and converting it into an electronic textile (e-textile) is proposed.

1.5. Thesis Organization

In this thesis, a study of extrusion printing electronics on textiles, specifically carbon fiber weaves, is presented. Extrusion printing is used to print electrodes on carbon fiber weaves to create two electronic devices. First, a self-heating carbon fiber composite that could be integrated in various structures including UAVs. Second, a damage sensor that senses and locates holes in 2 dimensions.

In chapter 2, the challenges of extrusion printing on woven textiles are discussed, and a method to overcome these challenges is presented. Extrusion printing is controlled by several parameters that are studied to reach optimal parameters for printing on carbon fiber weaves.

In chapter 3, the carbon fiber heating composite is demonstrated and evaluated. The carbon fiber heater composite is aimed towards being integrated in UAV wings for de-icing. The design approach of the heater is discussed, and the heater is manufactured and tested. A version of chapters 2 and 3 has been published in: Idris, M. K., Qiu, J., Melenka, G. W., & Grau, G. (2020). "Printing electronics directly onto carbon fiber composites: unmanned aerial vehicle (UAV) wings with integrated heater for de-icing". Engineering Research Express, 2. https://iopscience.iop.org/article/10.1088/2631-8695/ab8e24

In chapter 4, the carbon fiber damage sensor is demonstrated. Different designs for the damage sensor are proposed and compared to reach better sensing resolution and accuracy. The damage sensor is designed to have multiple electrodes in strategic locations that enable sensing in 2 dimensions and pinpointing the location of the potential damage. The sensor fabrication and design present multiple challenges to detect small changes in voltage measurements in different locations. Thus, a customized circuit that overcomes these challenges is designed and used for testing the damage sensor. A version of this chapter has been submitted as a journal paper: Idris, M. K., Naderi, P., Melenka, G. W., & Grau, G. "Damage Sensing and Localization in Carbon Fiber Composites Using Extrusion Printed Electronics".

In chapter 5, the main findings of this thesis are summarized and future research directions are suggested.

CHAPTER 2. PRINTING ON CARBON FIBER

A version of this chapter has been published in Idris, M. K., Qiu, J., Melenka, G. W., & Grau, G. (2020). "Printing electronics directly onto carbon fiber composites: unmanned aerial vehicle (UAV) wings with integrated heater for de-icing". *Engineering Research Express*, *2*. https://iopscience.iop.org/article/10.1088/2631-8695/ab8e24

2.1. Introduction

Extrusion printing, also known as dispenser printing, is a contactless nozzle-based printing method. It is digital, which means ink is extruded only when needed and does not require any masks. It works by applying pressure in an ink cartridge to dispense ink through the nozzle. Extrusion printing can be used to print stretchable and flexible conductors and passive circuit elements.[12], [57] Highly viscous inks are used in this process (approximately 10^3 to 10^6 cP) to prevent leakage through the nozzle.[11] This creates thick-layer patterns (~100 μm), which makes this process ideal for printing on textiles. Metal-based inks are the most commonly used inks in extrusion printing, such as silver ink made from silver flakes and a polymer binder dissolved in a solvent.[10] Compared to other printing methods like screen printing and inkjet printing, extrusion printing combines the desired attributes for printing on textiles, which include high viscosity ink, digital, print on demand, no mask. The main challenge of extrusion printing on textiles is that this method requires the nozzle to be close to the substrate for continuous printing.

Extrusion printing faces many challenges when used to print on textiles, chief among is the fact that it requires the nozzle to be close to the substrate (80 – 150 μm). The proximity of the nozzle to the textile substrate results in the nozzle entangling in the fibers of the textile which could break the nozzle, and move or damage the textile. So far, no successful extrusion printing attempts on textiles have been reported.

2.2. Materials

Three different types of weaves were used: 12K Unidirectional weave (12K UD), 6K Twill weave and 3K Twill weave. The carbon fiber weaves were acquired from Sigmatex Ltd. The weaves have different thicknesses due to the different number of fibers in each tow (12K, 6K and 3K), which is essential information for extrusion printing. The Unidirectional and Twill weaves have different geometries as shown in Figure 2-1. In the Unidirectional case, all carbon fibers are aligned in the same direction with no fibers crossing over each other, however, there is a Nylon string used to keep the tows together. Twill weaves have orthogonal carbon fiber tows crossing over each other with a periodicity of two tows (2x2 Twill).

Extrusion printing on carbon fiber was achieved using a desktop printed circuit board printer (Voltera V-One PCB printer, Kitchener, ON). The nozzle size was 225 µm. The ink was a silver flake ink (120-07) from Creative Materials Inc. This ink's viscosity (26,000 - 30,000 cP) is high enough for extrusion printing. The printing pattern was designed using EAGLE, Autodesk.

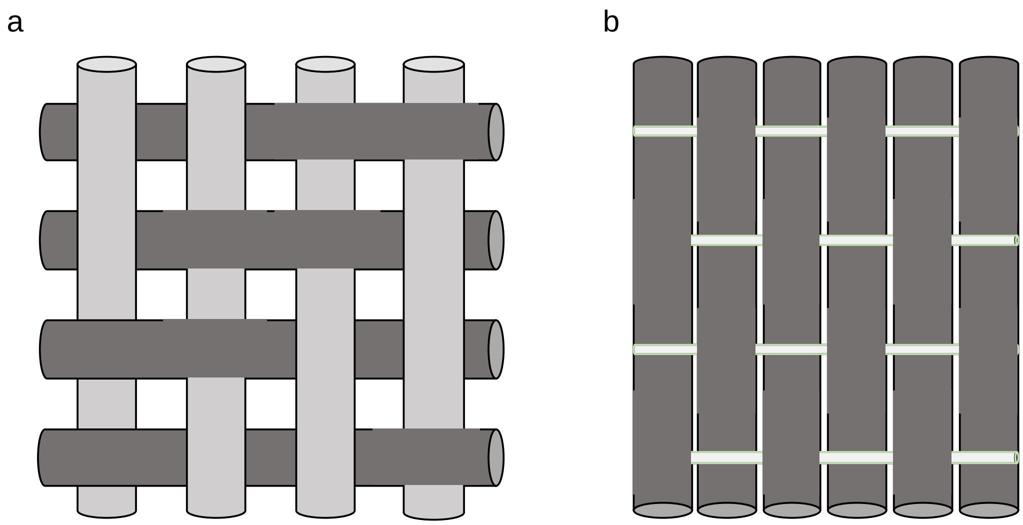

Figure 2-1. Illustration of different forms of carbon fiber weaves: a) Twill (2x2) weave with orthogonal fiber tows crossing over each other, b) Unidirectional weave with carbon fiber tows in only one direction; Nylon perpendicular strings used to keep tows together.

2.3. Overcoming the Challenges of Printing on Carbon Fiber

The V-One printer utilizes multiple steps for the printing process: probing, ink calibrating and printing. A sharp tip is used to probe the surface of the substrate in contact mode to determine the substrate position and height. This ensures consistency in print height and prevents the delicate nozzle tip from contacting the substrate and breaking in the printing phase. In the ink calibration phase, the cartridge is mounted, and the printer prints a test design on a glass substrate. The various printing parameters can be edited until the desired amount of ink is dispensed. In the printing phase, the pattern design is printed on the substrate by scanning the nozzle and controlling the pressure in the ink cartridge with a piston. Using this method and printer to print on carbon fiber weaves presents multiple challenges. The contact-based probe cannot be used with the textile as it can either bend the fibers and break them or penetrate between the fiber tows. Therefore, instead of probing the carbon fibers directly, the nozzle height above the underlying glass substrate was increased by the average thickness of the carbon fiber textile measured using a micrometer (Power Fist 0-1"). Additionally, the weave has large surface roughness and topography and there are many frayed fibers and tows, which can cause the nozzle to become entangled. To overcome this challenge, tension is applied to the carbon fiber weave while a clamping force is applied. Then, the weave is saturated with acetone which uses surface tension to mechanically adhere the fibers to the glass slide. After waiting for approximately 5 minutes to ensure that the acetone has fully evaporated and the weave has dried, the printing phase is initiated. An additional offset of 350 μm is added to the nozzle height above the nominal surface of the carbon fiber weave to prevent nozzle entanglement. The height offset is the minimum offset possible to safely print on the weave. As a result, the printing parameters had to be adjusted to print at this extreme nozzle height as discussed below. Finally, the pattern is successfully printed on the carbon fiber weave. This method can potentially be used to print on a wide range of textiles that have similar or lower surface roughness than the carbon fiber weaves used here.

2.4. Printing on Glass

Printing using the Voltera V-one printer has multiple printing parameters. To optimize these parameters, lines and squares were printed on glass while considering the constraints of the carbon fiber weaves as shown in Figure 2-2 (a). The squares and rectangles were printed using the built-in spiral pattern. The printed features were analyzed using a stylus profilometer as shown in Figure 2-2 (b). By integrating the area under the line of the profilomiter scans, the average area of lines was calculated and used to optimize the parameters. Then, optimized parameters, shown in Table 1, were used to print on the carbon fiber weaves.

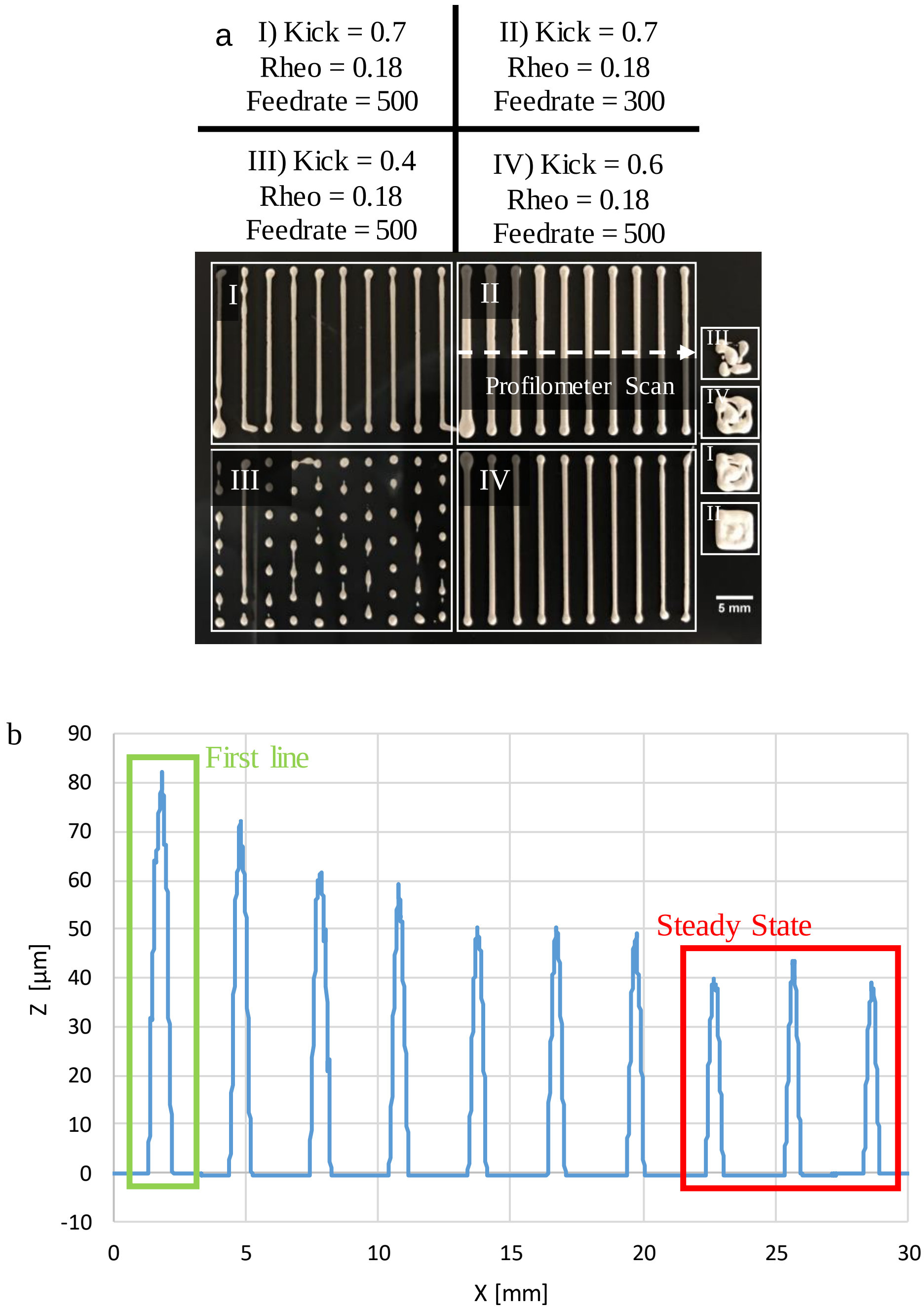
a
I) Kick = 0.7
Rheo = 0.18
Feedrate = 500
II) Kick = 0.7
Rheo = 0.18
Feedrate = 300
III) Kick = 0.4
Rheo = 0.18
Feedrate = 500
IV) Kick = 0.6
Rheo = 0.18
Feedrate = 500
I
II
III
IV
Profilometer Scan
5 mm
b
First line
Steady State
Z [µm]
X [mm]
90
80
70
60
50
40
30
20
10
0
-10
0
5
10
15
20
25
30

Figure 2-2. a) Line and square patterns printed on glass slide at a nozzle height offset of 350 µm. One can observe discontinuous lines when printing parameters are close to the default values (III). Increasing Kick increases the dispensed ink volume, but ink volume diminishes during the print if Rheological Setpoint is not increased as well (I, II, IV). In each print, the line on the left was printed first. Decreasing Feedrate leads to wider and thicker lines (II). b) Profilometry scan across printed lines with parameters: Nozzle height=350 µm, Kick=0.7 mm, Rheological Setpoint=0.18, Feedrate=300 mm/min. Cross-sectional area (ink volume per unit length) diminishes from the first line until steady state is reached.

The most relevant printing parameters that were studied are: Dispense height, Kick, Rheological Setpoint and Feedrate. Dispense height corresponds to the nozzle height offset from the substrate. Increasing the nozzle height results in a decrease in ink per unit length of lines (cross-sectional area of lines in profilometry scan) dispensed in steady-state as shown in Figure 2-3. This is a major problem for printing onto carbon fiber weaves where a large nozzle height is required due to the topography of the weave and to prevent the nozzle from becoming entangled in stray fibers. To compensate for this problem, the other printing parameters need to be adjusted. Kick and Rheological Setpoint control the pressure in the cartridge, thus controlling the amount of dispensed ink. The Kick parameter controls the stroke length of the dispensing piston. Increasing the Kick results in an increase in ink dispensed overall and especially in the first line as shown in Figure 2-4. This can overcome the reduction in ink flow due to the increased print height. However, the increased ink flow diminishes over time for larger prints. For example, when multiple lines are printed successively, later lines have less ink (see Figure 2-2 (b)). This is a problem when trying to print repeatable patterns over large areas such as on an aircraft wing. To solve this, the Rheological Setpoint parameter needs to be adjusted. The Rheological Setpoint corresponds to how the printer compensates for the flow rate over time. Increasing the Rheological Setpoint increases compensation and thus the amount of ink dispensed for every line as shown in Figure 2-5 and Figure 2-6. Feedrate corresponds to the nozzle XY-axis travel speed during dispensing. Increasing the Feedrate results in less ink per unit length of line as shown in Figure 2-7. This means there exists a trade-off between manufacturing throughput and line thickness. Above a threshold of 500 mm/min, lines were not continuous anymore. In addition to lines, squares were also printed and analyzed in terms of defects (holes). The dispensed ink volume follows the same trends and the same optimized printing parameters can be used.

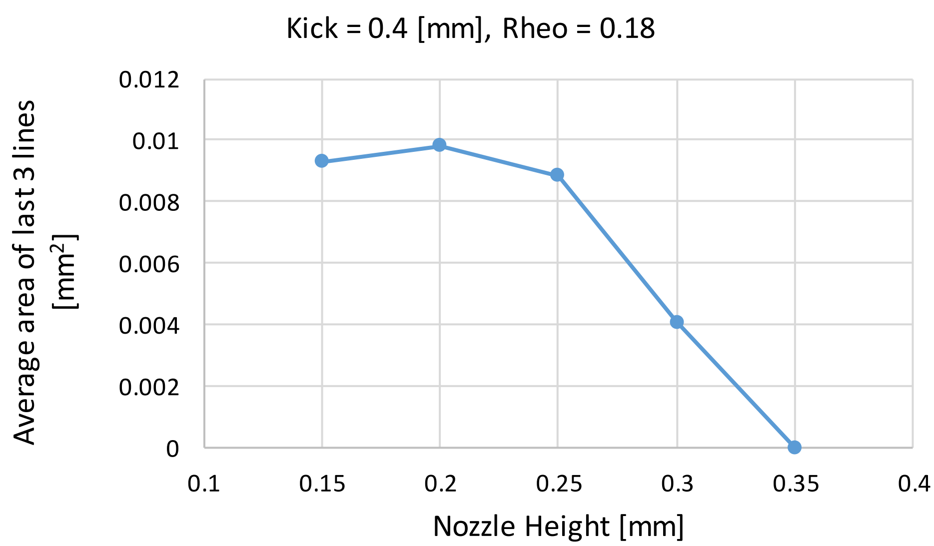

Figure 2-3. Effect of nozzle height on line area. Increasing nozzle height, as required to print onto rough carbon fiber weave, results in diminished ink flow with standard settings.

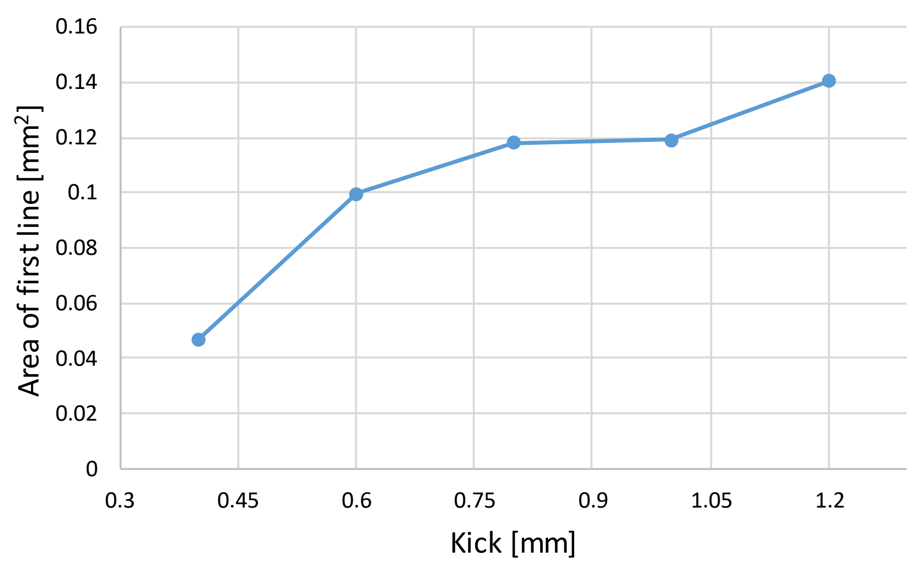

Figure 2-4. Effect of Kick on line area. Increasing Kick increases ink flow; however, predominantly for the first line in larger prints.

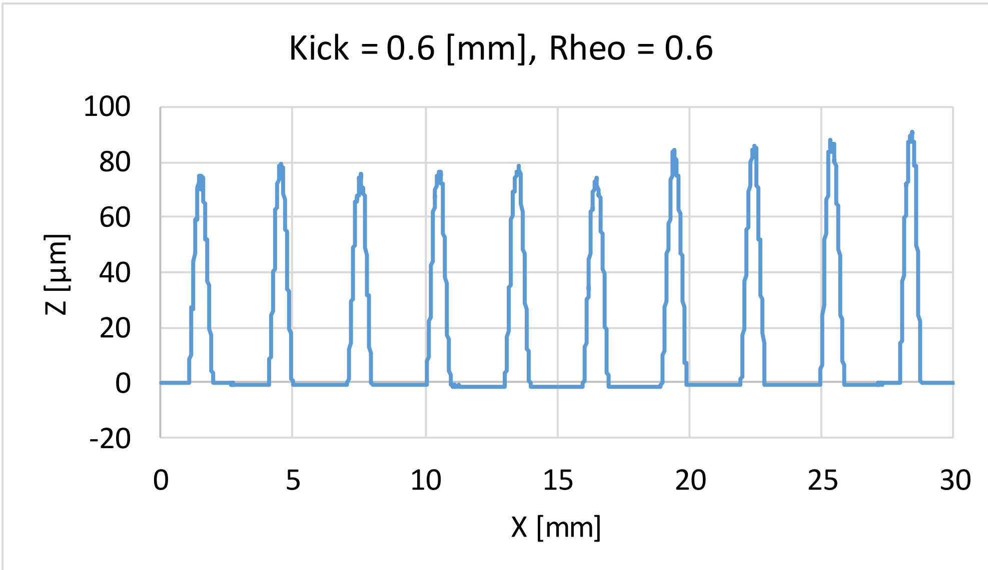

Figure 2-5. With higher Rheological Setpoint, diminishing ink flow during longer prints is compensated for, resulting in more uniform printing.

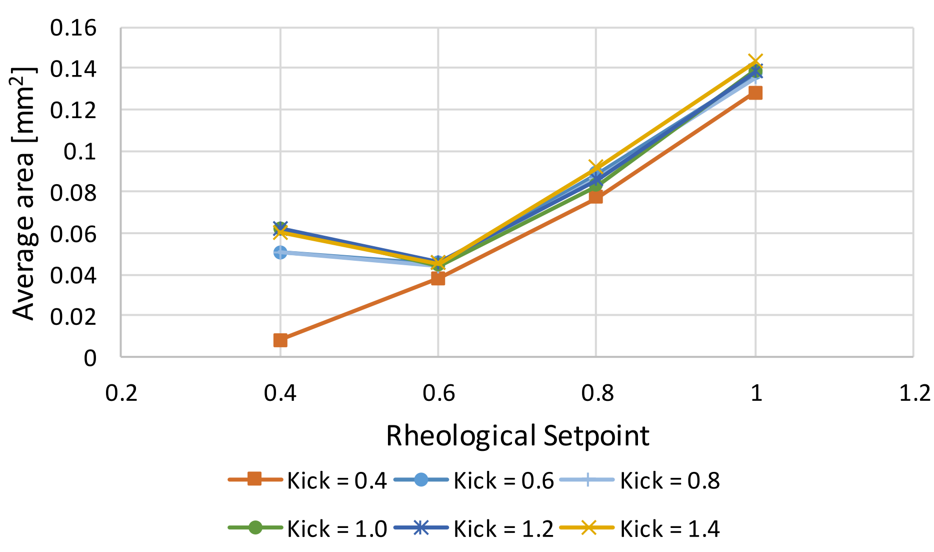

Figure 2-6. Effect of Rheological Setpoint parameter on steady-state line area.

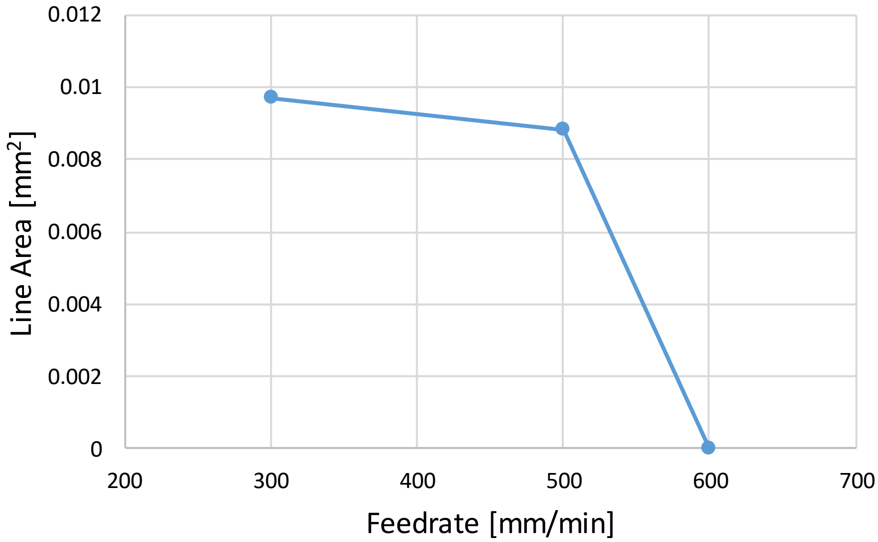

Figure 2-7. Effect of Feedrate on line area. The maximum Feedrate that gives working lines is 0.5 mm/min.

2.5. Extrusion Printing on Carbon Fiber

The insights gained by printing onto glass also apply to printing onto carbon fiber weaves. Figure 2-8 shows the same trends for individual lines. Kick and Rheological Setpoint need to be increased from default values to achieve consistent printing of sets of lines with the increased print height necessary to print onto rough carbon fiber weaves. Continuous lines can be achieved; however, pattern fidelity is deteriorated because of the topography of the carbon fiber weave. Bulges occur where the printed lines cross from one carbon fiber tow to the next or cross over the nylon yarns holding the unidirectional weave together. The optimized print parameters to print contacts on carbon fiber weaves are shown in Table 2-1. Figure

2-9 (a)-(d) show samples of the discussed devices with printed contacts on the different carbon fiber weaves (12K UD, 6K Twill, 3K Twill).

Table 2-1. Optimized printing parameters used in heater manufacturing.

PRINTING PARAMETER	VALUE
Nozzle offset from carbon fiber weave	350 µm
Kick	0.5 mm
Rheological Setpoint	0.5
Feedrate	500 mm/min

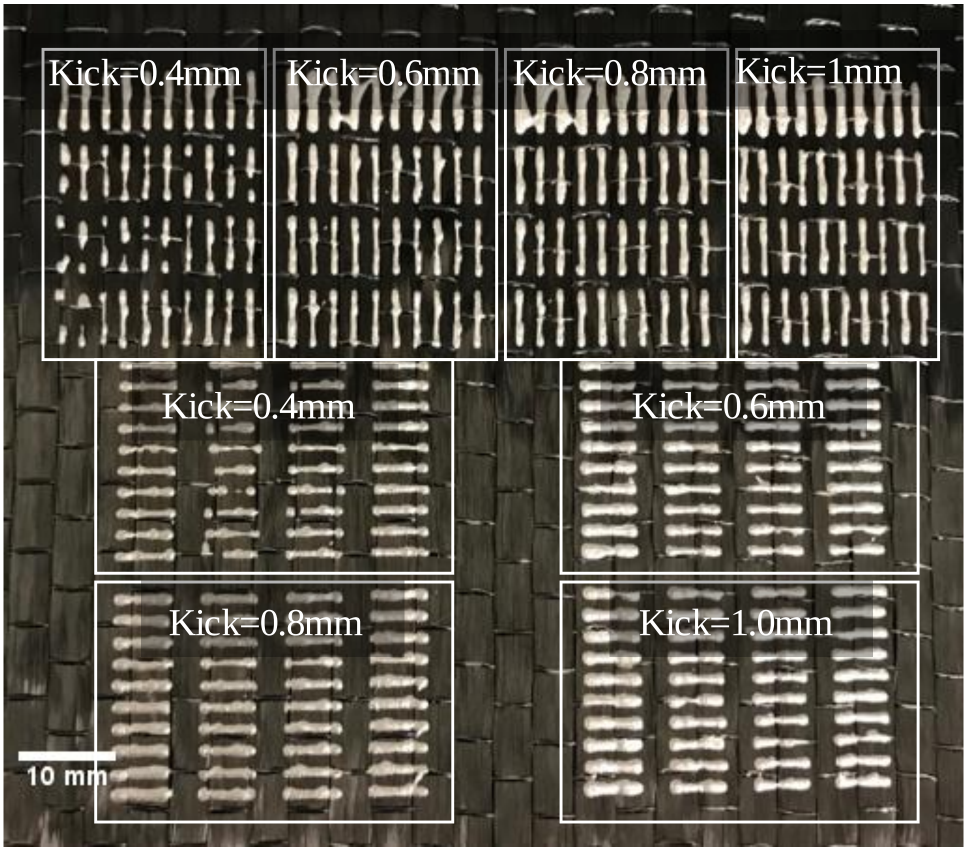

Figure 2-8. Blocks of individual lines printed on 12K UD carbon fiber in two directions using different Kick and Rheological Setpoint values. Rheo values from top to bottom and left to right: 0.4, 0.5, 0.6, 0.8. Similar trends can be observed as on glass. Lines can be continuous, but pattern fidelity is deteriorated by topography of CF weave.

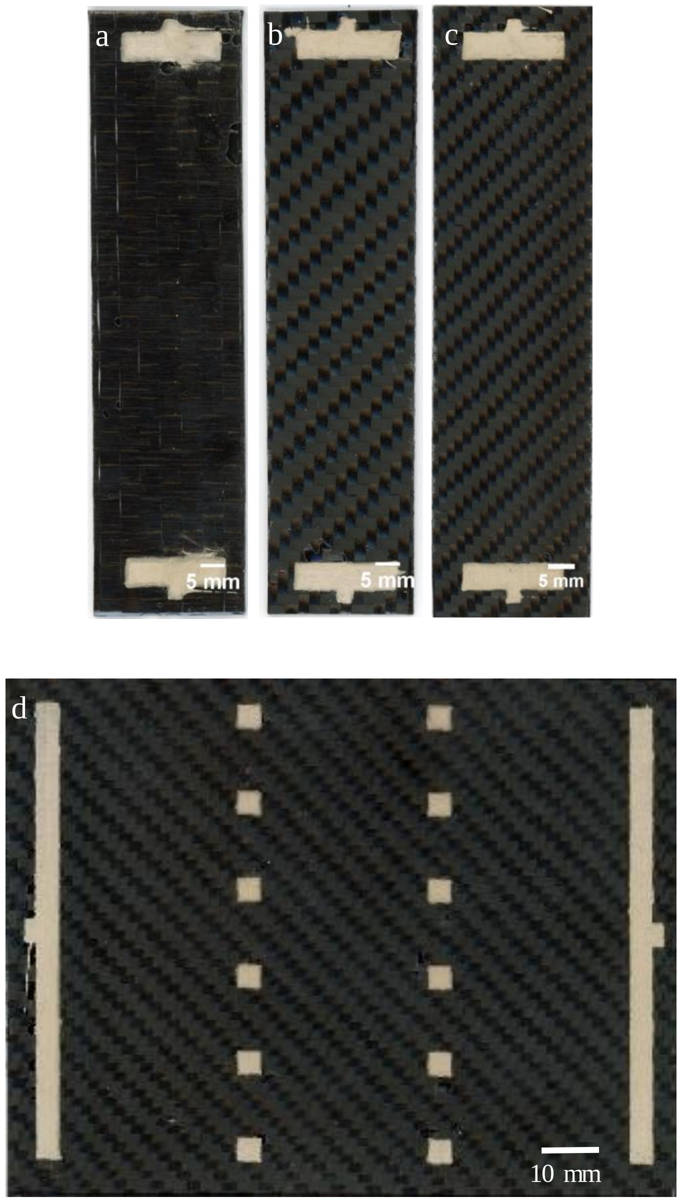

Figure 2-9. Printed patterns on woven carbon fiber. a) Heater design pattern printed on 12K UD carbon fiber weave. b) Heater design pattern printed on 6K Twill carbon fiber weave. c) Heater design pattern printed on 3K Twill carbon fiber weave. d) Damage sensor design printed on 3K Twill carbon fiber weave.

2.6. Conclusions

Printing electronics on textiles is a challenge because of the large surface roughness of textiles. This chapter presents a new method with the optimized parameters to use extrusion printing to print on textile composites, specifically, carbon fiber weaves. The standoff distance between the nozzle and the textile needs to be increased to avoid entanglement between the nozzle and the fibers. To nevertheless achieve good print quality and sufficient ink flow, the piston pressure needs to be increased whilst compensating for the loss in pressure throughout a print run. The printing parameter values used were: Nozzle height offset 350 μm; Kick 0.5 mm; Rheological Setpoint 0.5; Feedrate 500 mm/min. As a result, the manufacturing of the carbon fiber-based devices is repeatable and scalable. Furthermore, since extrusion printing is a contactless digital printing method, the proposed methods allow for the facile variation of the pattern design to create various types of electronic devices and circuits.

CHAPTER 3. CARBON FIBER HEATING DEVICE

A version of this chapter has been published in Idris, M. K., Qiu, J., Melenka, G. W., & Grau, G. (2020). “Printing electronics directly onto carbon fiber composites: unmanned aerial vehicle (UAV) wings with integrated heater for de-icing”. Engineering Research Express, 2. https://iopscience.iop.org/article/10.1088/2631-8695/ab8e24

3.1. Introduction

Unmanned Aerial Vehicles (UAVs) are increasingly being used to deliver items to remote areas and gather information.[17] However, they face challenges due to ice accretion on their wings. This greatly restricts the performance of drones in high altitudes and remote cold areas.[18] Aircraft icing occurs when water droplets from the air or clouds accumulate and freeze on the surfaces of an aircraft. Although icing occurs on large commercial transport aircrafts, icing has a greater effect on smaller aerial vehicles such as drones, commuter aircraft and small transport aircraft due to their size. There are several methods for de-icing aircraft wing. Electro-thermal systems can be used in small aircrafts on surfaces such as intake lips or helicopter rotors.[19] However, such de-icing solutions are not yet commercially available due to the young developing industry of UAVs.[21]

Carbon fiber composites are becoming ubiquitous in the UAV industry. They are being used to create propellers, wings and tubes that connect the body of a drone to its rotors.[23], [24] This is due to the attractive physical properties of carbon fiber such as excellent tensile properties, low density, high strength to weight ratio, high thermal and chemical stability, and good thermal and electrical conductivity.[13] Due to their electrical and thermal conductivity, carbon fiber can be used directly as the heating element in an electrical heater. This way, an aircraft wing can be heated without the need for a separately applied heater, such as a flexible heater on a plastic substrate.

In this chapter, it is proposed to exploit the electrical and thermal conductivity of carbon fiber to create electrical heating devices. Carbon fiber textiles are used as the heating element without major changes to common CFRP manufacturing processes. The added cost of the proposed carbon fiber heater is calculated by dividing the price of the amount of silver used over the heating area which is only 0.03$/cm^2.

3.2. Materials

Three different types of weaves were used: 12K Unidirectional weave (12K UD), 6K Twill weave and 3K Twill weave. The weaves have different thicknesses due to the different number of fibers in each tow (12K, 6K and 3K), which is essential information for extrusion printing. The thicknesses of the 12K, 6K and 3K weaves were measured using a micrometer (Power Fist 0-1”) and they roughly are 700 μm, 600 μm and 400 μm respectively. This rough measurement of the thicknesses is not accurate due to the complicated designs of the weaves, but it is adequate as a generalization for printing on the weaves. The Unidirectional and Twill weaves have different geometries. In the Unidirectional case, all carbon fibers are aligned in the same direction with no fibers crossing over each other. Twill weaves have orthogonal carbon fiber tows crossing over each other with a periodicity of two tows (2x2 Twill). The different geometries affect the electrical current and heat flow. Unidirectional limits current and heat flow to one direction aligned with the carbon fiber tows. The carbon fiber weaves were acquired from Sigmatex Ltd. The weaves were infused with 2000 laminating epoxy resin system 9 (Fibre Glast 2000 laminating and 2020 hardener). This epoxy is a room temperature two-part system that is used in the production of high strength structural parts in the space, automotive and structural industries.

LOCTITE Frekote 700-NC was used as a release layer on the mold plates and the 3D printed wing before placing the carbon fiber weave on them to create multiple interfacing layers that prevent the epoxy from adhering to the mold.

3.3. Heating Device Manufacturing and Characterization

Manufacturing the heating device is done in four steps. First, the designed silver pattern is printed on a 2D flat and dry carbon fiber weave, as discussed in chapter 2 and shown in Figure 3-1 (a). The weave is then put into an oven whose temperature is being ramped up to 150 ºC to cure the printed silver for 30 minutes. Then, the epoxy is mixed at the recommended ratio (4:1 Resin: Hardener) and infused into the carbon fiber weave, as shown in Figure 3-1 (b). In the third step, flat 2D and 3D devices are made. For the flat 2D devices, the weave is positioned between two polished stainless-steel plates. A mechanical press is used to apply pressure (3 tons of force) on the plates to force out excess epoxy resin and give a smooth finish to the carbon fiber composite, as shown in Figure 3-1 (c). The release layer is applied on the plates before adding the carbon fiber weave on them to prevent the epoxy from sticking to the mold. The epoxy resin infused weaves were left to cure at room temperature for 24 hours. Finally, the carbon fiber composite is delaminated from the plates, as shown in Figure 3-1 (d). In the case of the 3D devices, the first two steps are repeated (printing silver onto CF and infusing with epoxy). In the third step, a Clark-Y wing is 3D printed and used as a mold. This wing design was selected for this proof of concept since it is commonly used in small aircraft. It also has a smooth profile with curvature within the bending limits of the cured silver contacts.[57] The carbon fiber weave is wrapped over the mold, and pressure is applied using heat-shrink tape wrapped over the weave, as shown in Figure 3-1 (e). The release layer is applied on the 3D printed wing before putting on the carbon fiber weave to prevent the epoxy from sticking to the mold. The epoxy resin infused weaves are left to cure in room temperature for 24 hours. The final 3D wing is shown in Figure 3-1 (f). The epoxy covering the printed silver electrodes is burnt off using a soldering iron at 450 ºC in strategic locations, making it possible to connect to the silver electrodes. Figure 2-2 (a), (b), (c) show the final flat heater devices manufactured using the different carbon fiber weaves (12K UD, 6K Twill, 3K Twill). Figure 3-2 (a), (b) show the 3D wing structure with three printed heaters.

Electrical measurements and current injection were performed using a DC current-voltage source measure unit (KEITHLEY 2602B SYSTEM SourceMeter®). Heat images were obtained with an infrared camera (FLIR A6751sc).

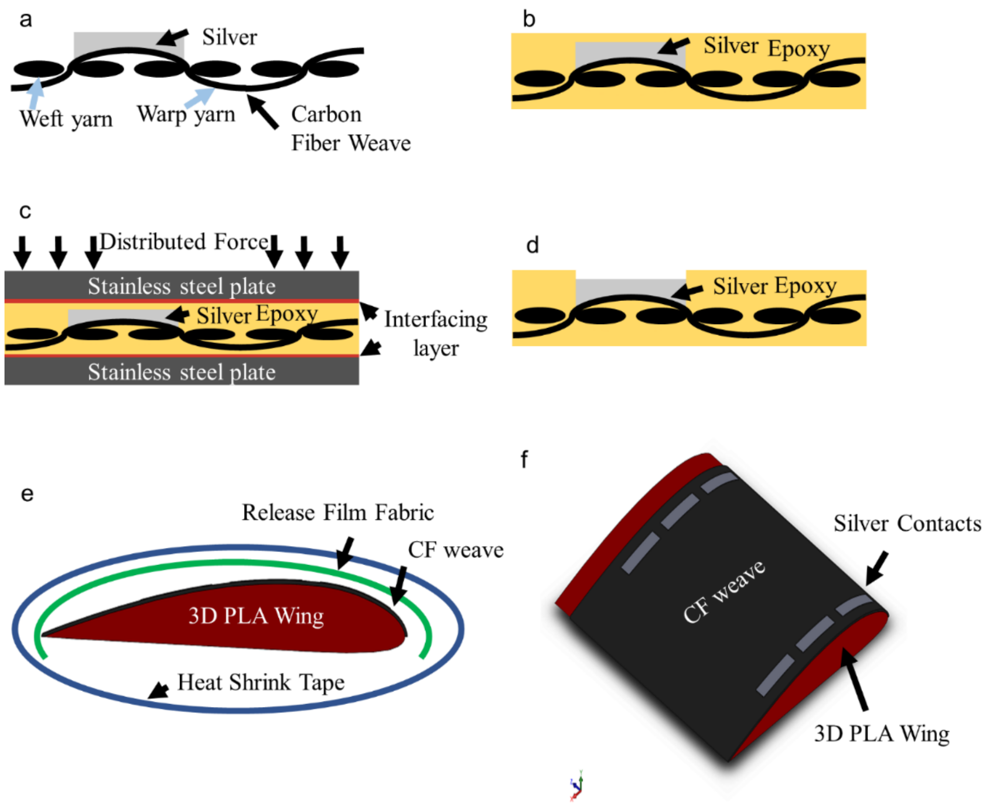

Figure 3-1. Heater Manufacturing Steps. a) Print pattern on dry carbon fiber weave (cross section); b) Infuse weave with epoxy. For flat device: c) Apply force and cure device in room temperature; d) Peal off, then melt epoxy covering silver pads. For 3D device: e) Wrap carbon fiber weave around mold and apply force using heat-shrink tape; f) Remove tape and then melt epoxy covering silver pads.

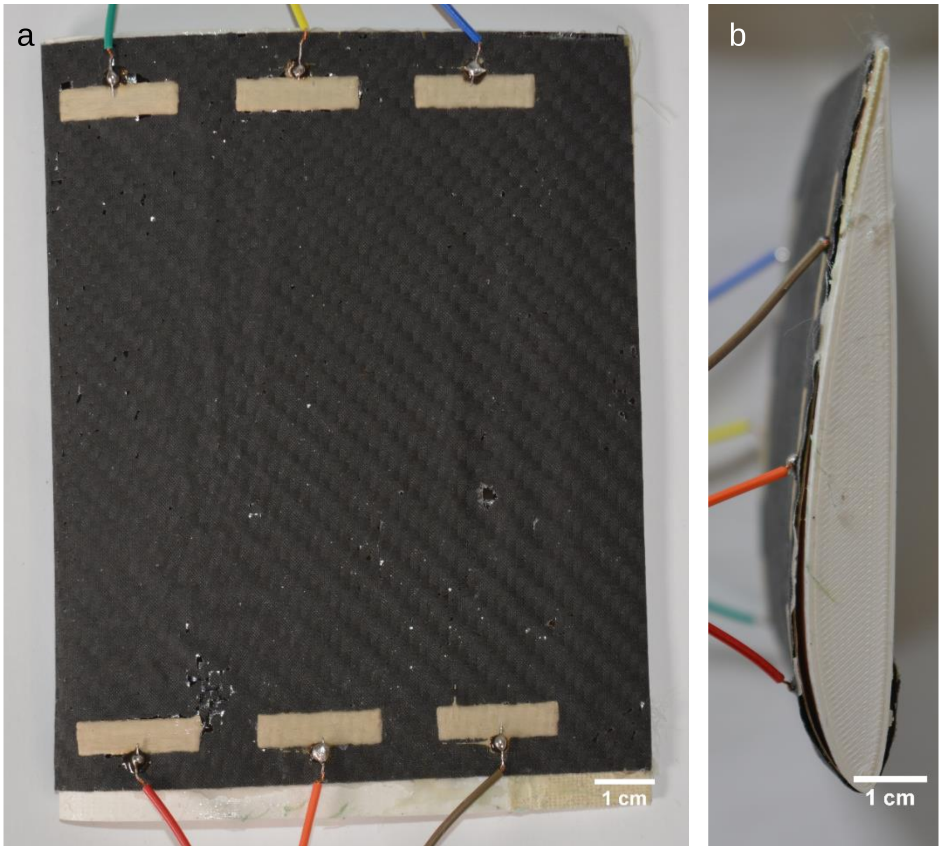

Figure 3-2. 3D wing structure a) Three fully manufactured 3D heater devices on a wing mold with 3K Twill. b) Profile of 3D wing with integrated heaters.

3.4. Designing the Pattern

Silver electrodes are printed on the carbon fiber weaves to produce a large-area heater. The electrodes are used to run an electrical current through the weaves resulting in power dissipation in the form of heat. It is essential to design the device for maximum power consumption and heat generation in the carbon fiber rather than the silver contacts to achieve maximum ration of power consumed in the carbon fiber to input power ($P(L)$%). Three main parameters were considered to design the printing pattern: The width of the silver electrodes (W_{Ag}), the length of the silver electrodes (L) and the distance between the two electrodes (W_{CF}) as shown in Figure 3-3. As voltage is dropped over the electrodes, the voltage across the carbon fiber heater diminishes with increasing distance from the point of current injection (distance x in Figure 3-3). Consequently, the electrical power dissipated in the carbon fiber, which is converted to heat, is lowest at the opposite end of the electrodes ($x=L$). To quantify this non-uniformity, we calculate ($P(L)$%) at the end of the electrodes i.e. the power consumed in the carbon fiber per unit width and converted to heat at $x=L$ as a percentage of the power consumed at $x=0$. The silver electrodes and the carbon fiber weave are treated as distributed resistances and the differential equations relating voltage and current as a function of position are solved to calculate ($P(L)$%) of the heater as a function of electrode length as shown in equations (1-3). The full derivation can be found in the Appendix A. R_{Ag} is the resistance of the silver electrode per unit length and R_{CF} is the resistance of the carbon fiber weave per unit width. t_{Ag} and t_{CF} are the thicknesses of the silver electrodes and carbon fiber weave respectively. ρ_{Ag} (0.3×10^{-4} Ω.cm) is the electrical resistivity of the silver electrodes and ρ_{CF} (23×10^{-4} Ω.m) is the resistivity of the carbon fiber.

$$R_{Ag} = \rho_{Ag}/(t_{Ag} \times W_{Ag}) = 3 \times 10^{-3}\Omega \,/\, W_{Ag} \tag{3-1}$$

$$R_{CF} = \rho_{CF} \times W_{CF}/t_{CF} = 3.3 \times 10^{-2}\Omega \times W_{CF} \tag{3-2}$$

$$P(L)\% = \frac{4\,exp\left(2L\sqrt{2R_{Ag}/R_{CF}}\right)}{\left(1+exp\left(2L\sqrt{2R_{Ag}/R_{CF}}\right)\right)^2} \tag{3-3}$$

As shown in Figure 3-4, Figure 3-5 and Figure 3-6, (*P(L)*%) increases with increasing width of the silver electrodes (W_{Ag}) and distance between the two electrodes (W_{CF}). At the same time, it decreases with increasing length of the silver electrode (*L*). Better (*P(L)*%) is achieved when the resistance of the silver electrodes is small compared with the resistance of the carbon fiber heating element because these resistances are connected in series acting as a voltage divider. By maximizing the resistance of the carbon fiber heater relative to the resistance of the electrodes, it is ensured that more of the input voltage and power are dropped across the heater rather than the electrodes. This design assumes the current is injected from one side of the electrodes. However, injecting the current in the middle of the electrodes allows for doubling the length of the electrodes (*L*), hence, creating a larger area heating device. The printing area of the V-One printer limits the maximum extent of W_{CF}. Considering this, the design dimensions were set to W_{Ag} = 5 mm, W_{CF} = 100 mm and *L* = 10 mm (from midpoint of electrode) as shown in

Figure 3-7 giving a ($P(L)$%) of 96%. Further improvements will be possible with a larger print area and thus larger W_{CF}. Printing multiple silver layers could also potentially improve ($P(L)$%) by increasing silver thickness t_{Ag}, reducing R_{Ag} and consequently increasing $P(L)$% according to equations (1) and (3). These equations, however, do not account for the contact resistance created between the silver electrodes and the carbon fiber.

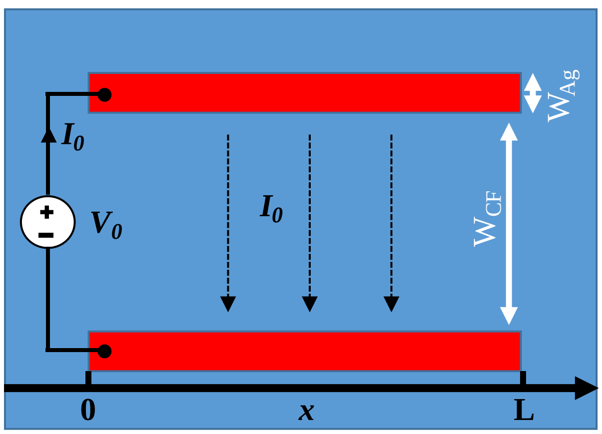

Figure 3-3. Printing pattern design parameters and electrical configuration with current injection on one side at x=0. Coordinate x is defined along the length of electrodes.

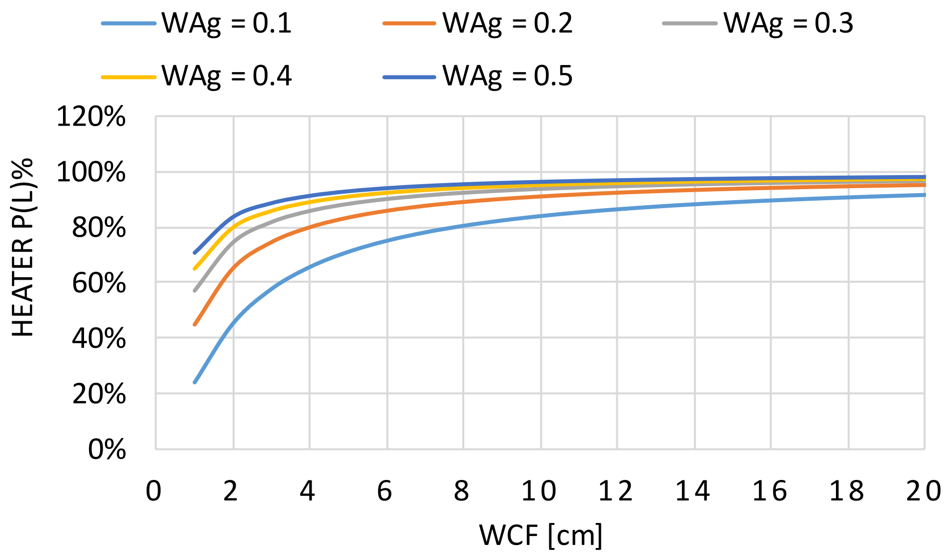

Figure 3-4. Effect of W_{Ag} on ($P(L)$%), L held constant at 1 cm.

(all units in legends in cm)

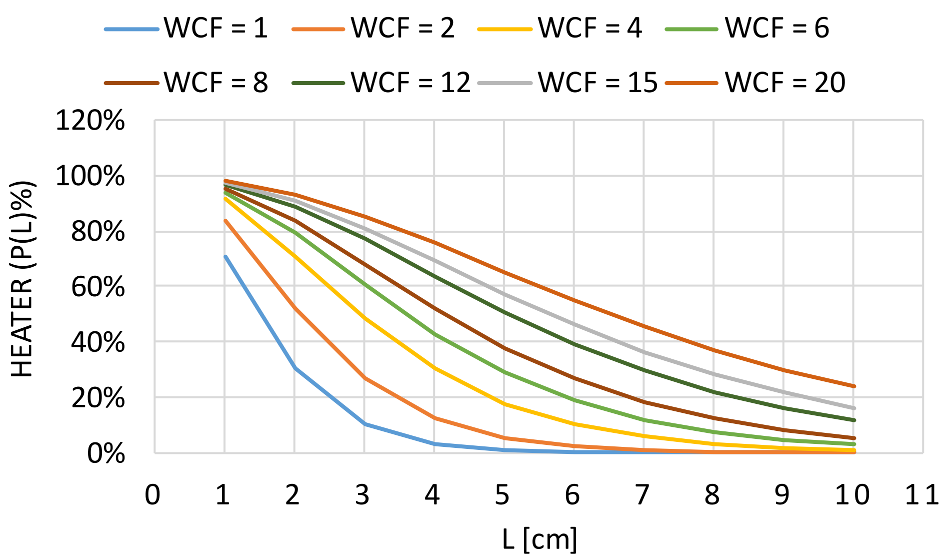

Figure 3-5. Effect of W_{CF} on ($P(L)$%), W_{Ag} held constant at 0.5 cm.

(all units in legends in cm)

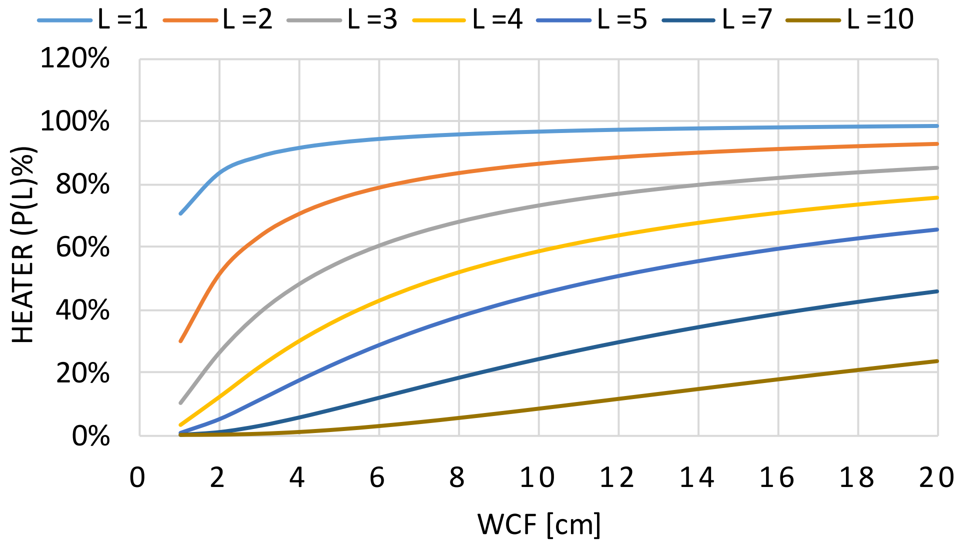

Figure 3-6. Effect of L on (*P(L)*%), W_{Ag} held constant at 0.5 cm.
(all units in legends in cm)

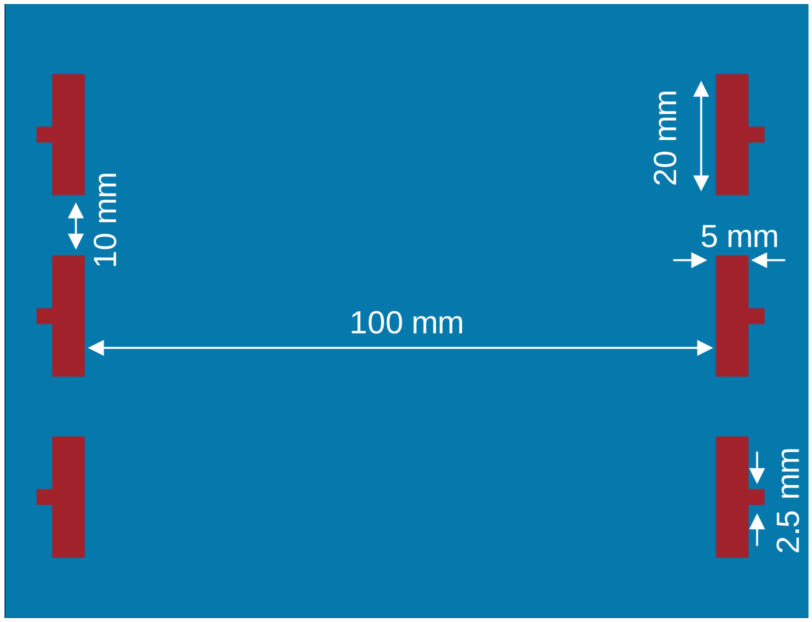

Figure 3-7. Printing pattern design and dimensions of the final heater in EAGLE containing three heaters arranged vertically. Current is injected into the pads at the center of the electrodes and flows horizontally.

3.5. Electrical and Heat Measurements

After the flat devices were manufactured, their electrical resistance was measured using the 4-point probe technique by injecting current in the outer side of the silver electrodes and measuring voltage at the inner side of the same electrodes.[58] The resistance measurement for all samples was approximately 1.1 Ω. Furthermore, the devices were connected to a current source, and an infrared camera was used to measure the temperature of the device. The amount of heat produced by the device corresponds to the electrical power consumed in the carbon fibers, which is proportional to the resistance of the device and the square of the input current. A current sweep was applied to all devices. Figure 3-8 shows that the device could operate as high as 108 ºC using a 3A current source, which is sufficient for de-icing. Lower current levels can likely be used to save energy depending on the severity of the ice conditions; however, this may not be necessary if de-icing is done on the ground with access to external power. Figure 3-9 (a), (b), (c) show that the orientation of the carbon fiber weave and the number of fibers in each tow influence the current and heat flow in the device. The Unidirectional weave (12K UD) exhibits a high degree of anisotropy. Electrical current is conducted along individual fiber tows, but conduction is minimal across different tows. Similarly, heat is not conducted well between tows. Tows are aligned with the direction of current flow to achieve electrical conduction between the electrodes. As a result, a hot zone can be observed at the center of the device with cold zones at the edges. The heat does not spread uniformly over the Unidirectional weave. Conversely, the Twill weaves have carbon fibers running in two orthogonal directions. The electrodes are printed such that one set of fiber tows is aligned with the direction of electrical current flow. Heat can spread along orthogonal fibers leading to a much more uniform heat distribution. 3K Twill has smaller fiber tows than 6K Twill, which again gives a more uniform heat distribution. Figure 3-10, Figure 3-11 and Figure 3-12 show the temperature profile along horizontal cuts at the center of the devices for different current values, again showing larger non-uniformity for the unidirectional weave. Figure 3-13, Figure 3-14 and Figure 3-15 show the temperature profile along vertical cuts at the center of the devices for different current values. A heater with long electrodes (10 cm) was also printed to confirm the modelling in section 3.4 and as expected did not perform well. Only minimal heating can be observed close to the point of current injection on the right side of Figure 3-16. Finally, a current of 3 A, which was the limit of our current source, was supplied to the 3D wing containing three separate heaters (1 A per heater), and the heat images were taken using the same apparatus used for the flat 2D devices. The temperature at the center of the wing reached 35 °C, which is comparable to the individual flat heaters for the same current of 1 A per heater. Figure 3-17 (a) shows the temperature distribution in the 3D wing device and Figure 3-17 (b) shows the temperature distribution at the center of the wing away from the electrodes. Some non-uniformity can be observed corresponding to the three heater devices. This could potentially be improved by optimizing the electrode geometry further, for example by placing electrodes closer to each other. Current and heat crowding close to the electrodes is more apparent in the larger CF sheet of the wing compared with individual flat heaters, but this does not significantly affect heating at the center of the wing where the de-icing would occur. These devices were created using a single layer composite that could warp with high temperatures. Manufacturers use different methods to account for this effect in multi-layer composites.

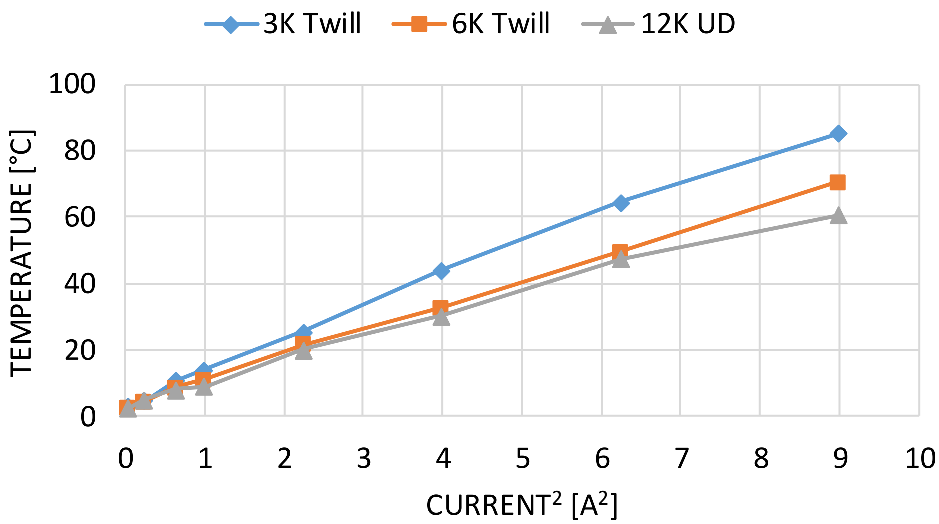

Figure 3-8. Heater temperature increases with the square of electrical current as expected for Joule heating. Temperature was averaged over a region of interest at the center of the heater (2 cm x 2 cm). Values above room temperature.

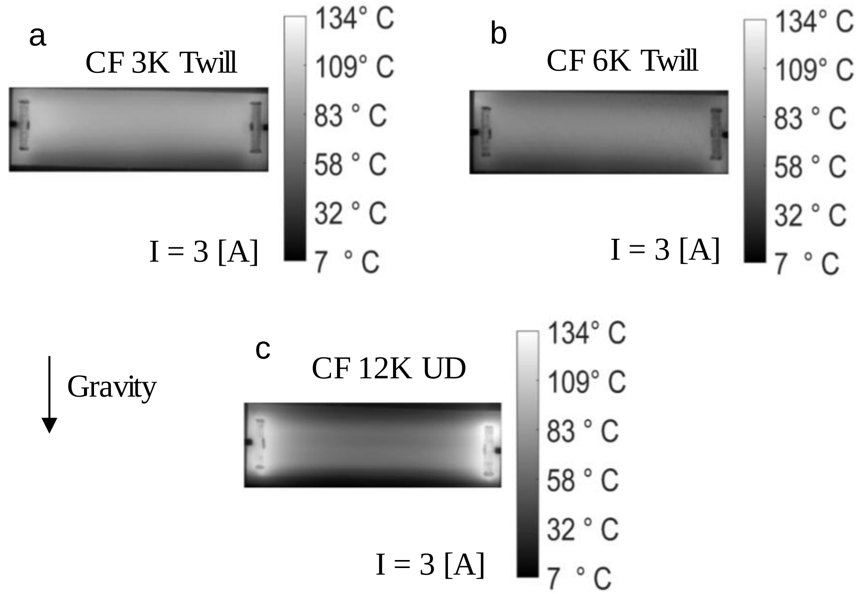

Figure 3-9. IR images of flat heaters. Values above room temperature. a) IR image of 3K Twill CF weave exhibiting good uniformity. b) IR image of 6K Twill CF weave. c) IR image of 12K UD CF weave exhibiting reduced uniformity.

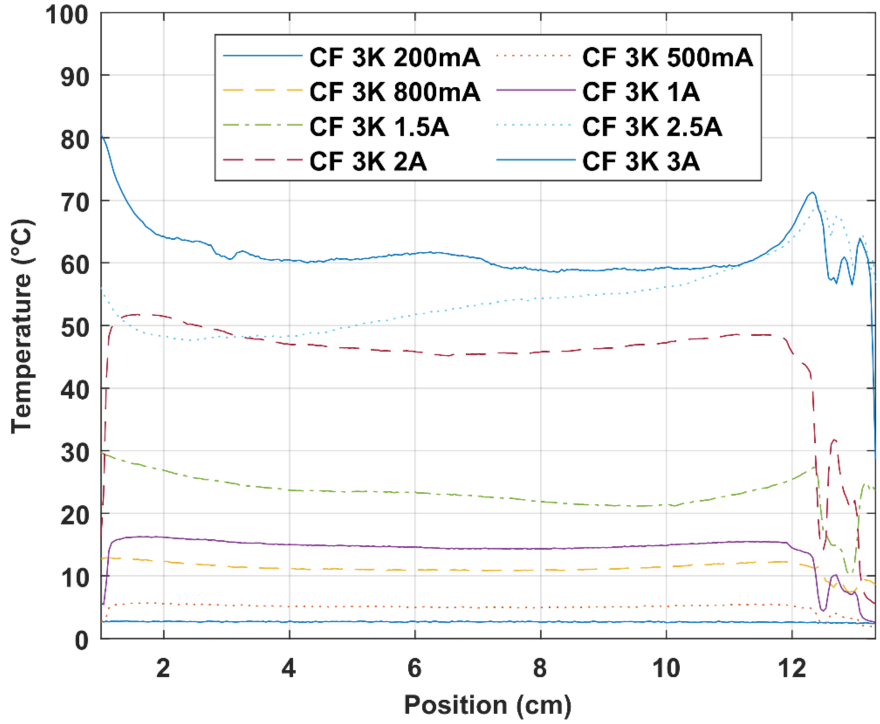

Figure 3-10. Horizontal cut of 3K Twill CF weave temperature response for different electrical currents. Values above room temperature.

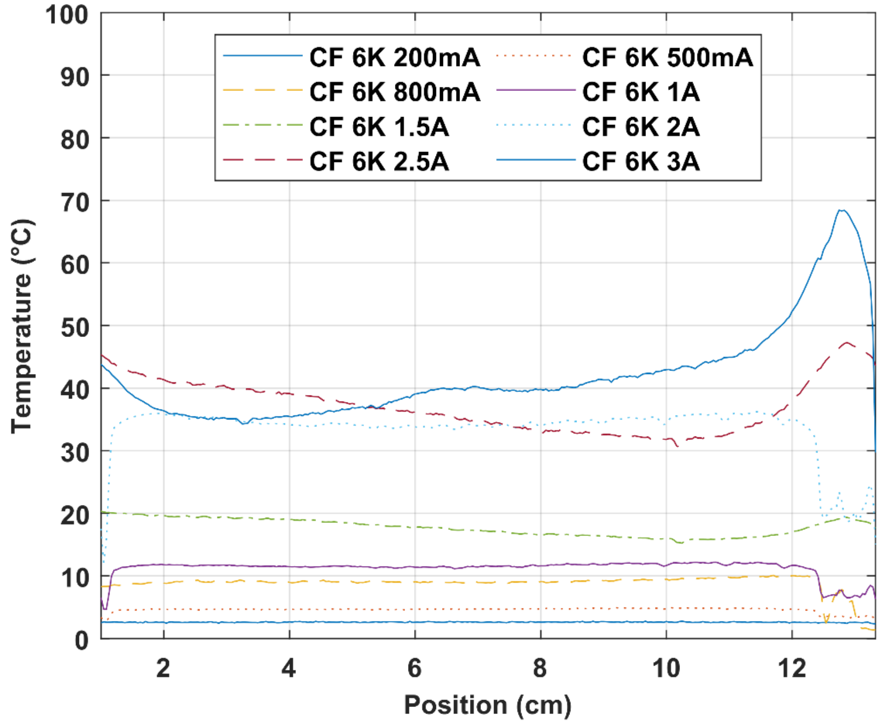

Figure 3-11. Horizontal cut of 6K Twill CF weave temperature response for different electrical currents. Values above room temperature.

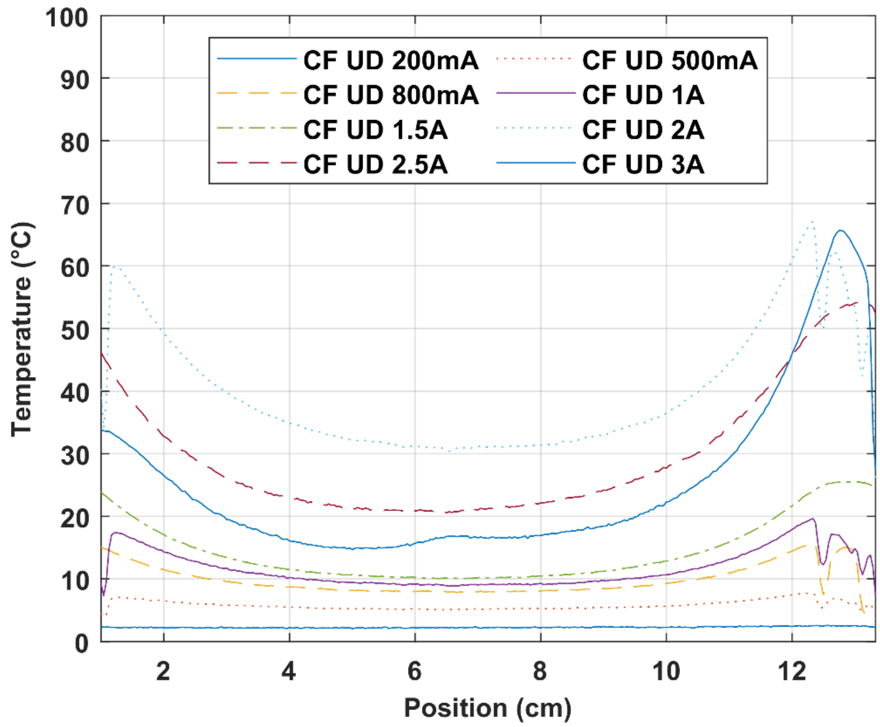

Figure 3-12. Horizontal cut of 12K UD CF weave temperature response for different electrical currents. Values above room temperature.

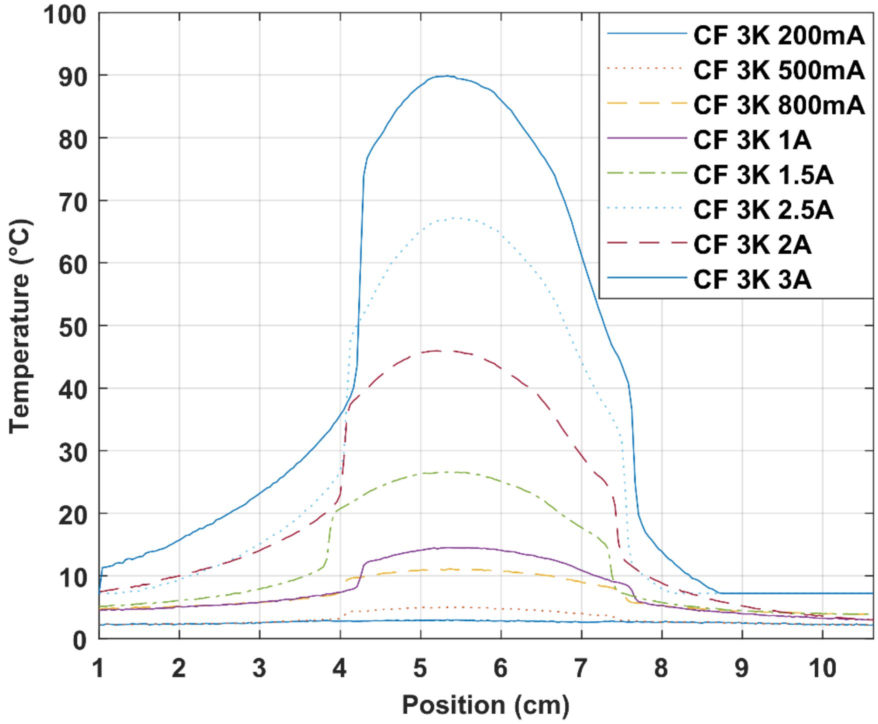

Figure 3-13. Vertical cut of 3K Twill CF weave temperature response for different electrical currents. Values above room temperature.

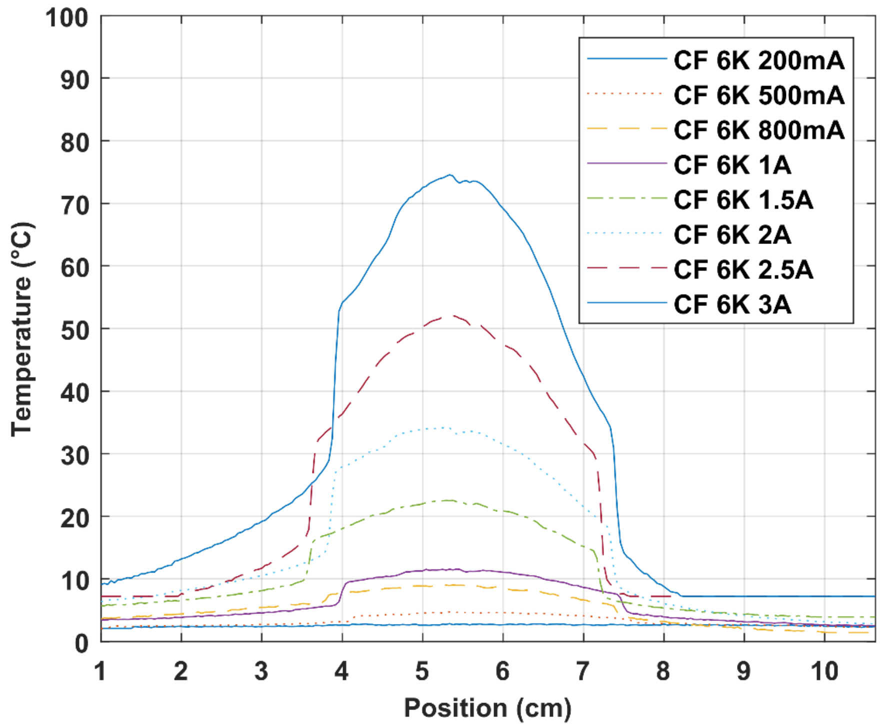

Figure 3-14. Vertical cut of 6K Twill CF weave temperature response for different electrical currents. Values above room temperature.

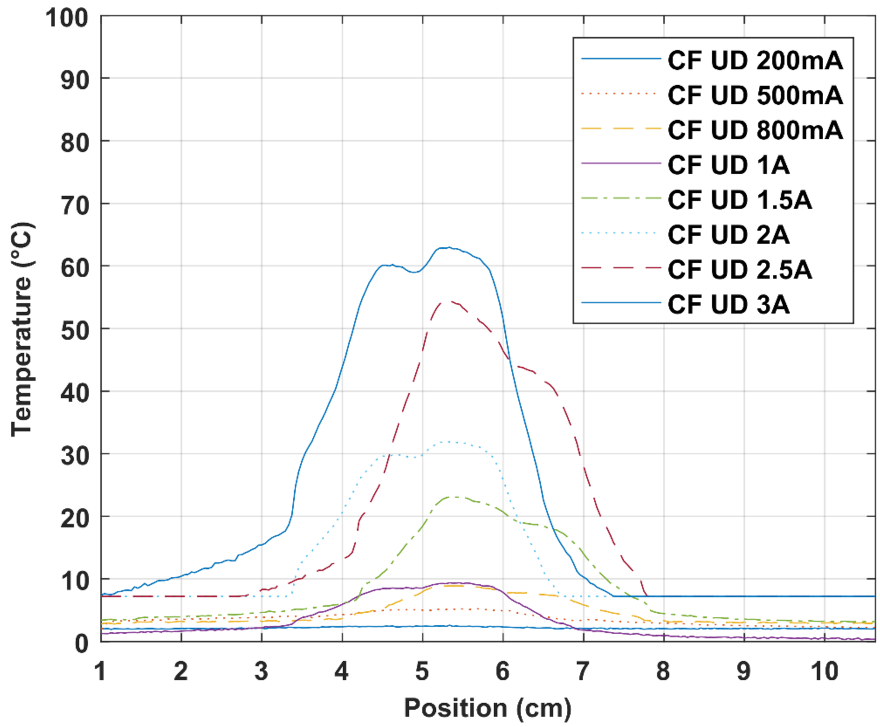

Figure 3-15. Vertical cut of 12K UD CF weave temperature response for different electrical currents. Values above room temperature.

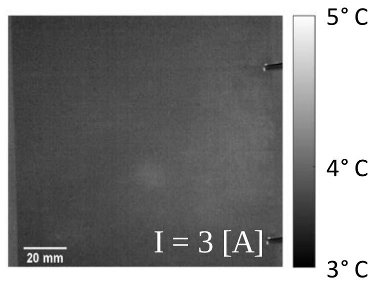

Figure 3-16. IR image of wide heater with single set of two long electrodes extending horizontally across the sheet (L = 10 cm). Only minimal heating close to the point of current injection (right) can be observed. Values above room temperature.

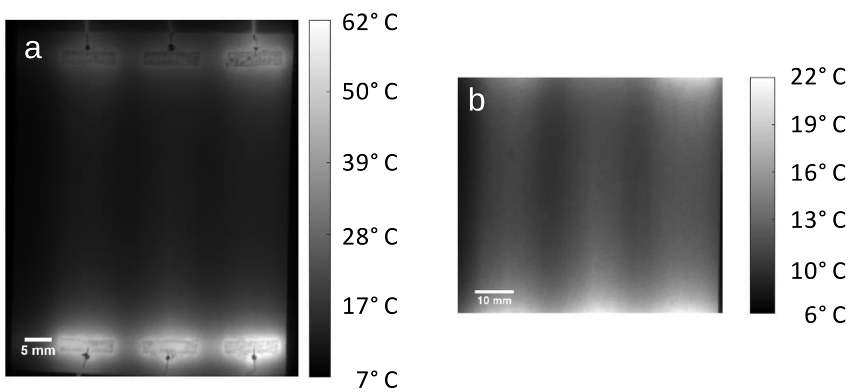

Figure 3-17. IR images of 3D wing heaters. Values above room temperature. a) IR image of 3D wing using 3K Twill CF weave with 1A of current per heater. b) IR image of the center region of the 3D wing shown in (a). The entire wing is heated with some temperature non-uniformity in between heaters.

3.6. Conclusions

This work exploits the electrical and thermal conductivity of carbon fiber to create self-heating composites that could be integrated into UAVs for de-icing. The manufacturing of the integrated heating devices is based on commonly used composites manufacturing methods with the addition of a printing step to create electrical contacts. The devices were manufactured, and temperature measurements were taken using an IR camera. Results show that the heating devices have been successfully fabricated and can achieve high temperatures suitable for melting ice on UAVs. The 3K and 6K Twill weaves show similar behavior where the heat spreads uniformly over the area between the two electrodes. In contrast, in the 12K Unidirectional weave the heat generated along the tows spreads less to the adjacent tows. Thus, the 3K and 6K Twill weaves are preferred for this integrated heater.

CHAPTER 4. CARBON FIBER DAMAGE SENSOR

A version of this chapter has been submitted as a journal paper: Idris, M. K., Naderi, P., Melenka, G. W., & Grau, G. "Damage Sensing and Localization in Carbon Fiber Composites Using Extrusion Printed Electronics".

4.1. Introduction

Another application for printed electronics integrated with carbon fiber composites is Structural Health Monitoring (SHM). SHM is used to detect damage and deformation in advanced engineering structures. This is achieved by introducing sensors that monitor the different physical aspects of a structure.[36] SHM is used in many industries, including mechanical, civil, and aerospace, to monitor damage in both products and manufacturing infrastructure, where detecting damage has life-saving and economic impacts.[38], [39]

Alterations introduced to a structure, such as holes, cracks, or corrosion, are considered damage that negatively affect the performance of the structure.[37] SHM is achieved using a system that compares the damage state of the structure to a previous undamaged state.[38]. SHM sensors integrated with textile composites enable in-situ wide-area sensing. In addition, they can be integrated with common manufacturing processes.[46] Most prevalent among textile composites are carbon fiber composites that are commonly used to reinforce structures such as aircraft, vehicles, bridges, and other concrete structures.

In this chapter, woven carbon fiber textiles are used as the primary sensing element to detect damage within them. The damage sensors are fabricated using conventional CFRP manufacturing processes with the addition of extrusion printing as discussed in chapter 2. Furthermore, this chapter discusses the designing steps to create a 2D wide-area self-sensing carbon fiber composite. This digital sensor can detect different sizes of holes as damage for structural health monitoring of composites. This damage sensor could be integrated into many structures as one of their layers or simply applied to their surfaces.

4.2. Materials

The printing patterns were designed using EAGLE, Autodesk. A low temperature (<205 °C) solder wire from VOLTERA was used to solder copper wires to the silver in the carbon fiber composite. All carbon fiber weaves were acquired from Sigmatex Ltd. The type used was 3K twill weaves. These weaves have 3,000 fibers in each tow. The epoxy infused into the weaves was the 2000 laminating epoxy resin system 9 from Fibre Glast (2000 laminating and 2020 hardener), which is a room temperature two-part system. The epoxy was mixed in the recommended weight ratio (4:1 Resin: Hardener). Polished stainless steel plates were used to give the composite a smooth finish. LOCTITE Frekote 700-NC was used as a release layer on the plates to create multiple interfacing layers that prevent the epoxy from adhering to the plates.

4.3. Damage Sensor Manufacturing

The sensor device was manufactured in four steps following similar steps as the heater device manufacturing discussed in chapter 3. A schematic of the manufacturing process is shown in Figure 4-1. In the first step, Figure 4-1 (a), (b), the desired silver pattern is printed on a dry carbon fiber weave using the printing method described in chapter 2. Then, the silver was cured in an oven, which was ramped to 200 ºC, for 60 minutes. After removing the weave from the oven, it was infused with the epoxy resin (Figure 4-1 (c)) and sandwiched between two polished stainless steel plates. Pressure was applied on the plates (3 tons of force) using a mechanical press (MAXIMUM 10-Ton Shop Press) to ensure a smooth finish and provide compaction to the woven yarns, as shown in Figure 4-1 (d). The composite was left in this state to cure for 24 hours. Next, the composite was delaminated from the steel plates. The epoxy covering the silver electrodes was burnt off using a soldering iron at 450 ºC. Jump wires were then soldered to the electrodes to be able to connect it to the breadboard and the rest of the circuit as shown in Figure 4-1 (e).

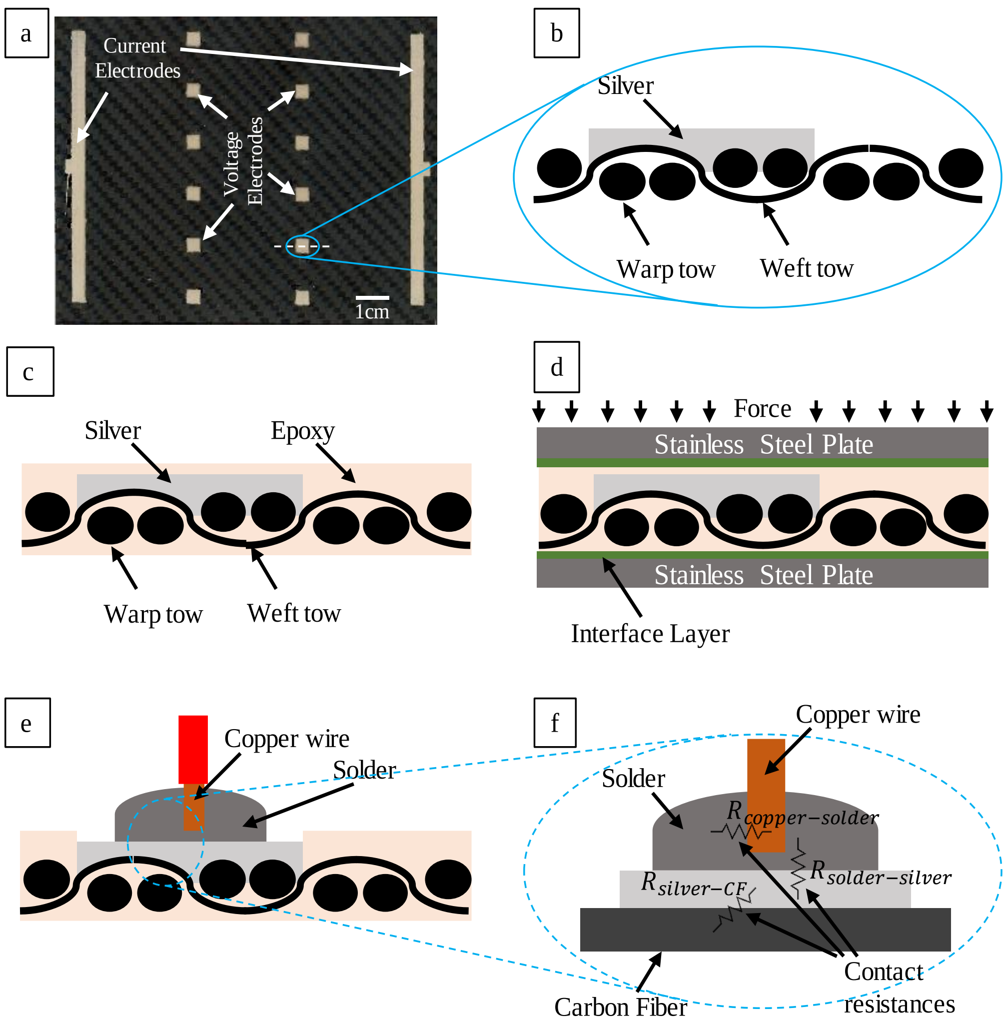

Figure 4-1. Manufacturing steps of the carbon fiber damage sensor using 3K twill carbon fiber weave, epoxy resin, and silver ink. a) Photo of carbon fiber weave with printed contacts. Long bars are used for current injection. Smaller square electrodes are used for voltage measurement at different positions to locate damage. Illustration of manufacturing steps of carbon fiber damage sensor: b) Cross-sectional view of printed contacts on carbon fiber. c) Infusing carbon fiber

weave with epoxy resin. d) Curing under pressure from mechanical press. e) Burning the epoxy off silver pads and soldering copper wires to them, which creates a series of contact resistances shown in (f).

4.4. Measurement and Data Acquisition Circuit

A circuit was created to collect and process the electrical measurements from the carbon fiber composite. The circuit combines the Kelvin Double Bridge 4-point probing method, digital multiplexing, and a data acquisition (DAQ) unit, as shown in Figure 4-2. To measure small impedance variations in piezo-resistive sensors, a Wheatstone bridge circuit is commonly used.[59] The Kelvin Double Bridge is an alteration of the Wheatstone bridge that includes an extra set of ratio resistor arms that provide higher measurement accuracy and enable the detection of even smaller resistance variations.[60] The six resistors of the Kelvin Double Bridge shown Figure 4-2 are $R_1, R_2, R_3, R_1', R_2'$ and the carbon fiber composite (R_x). The resistance of the carbon fiber weave was measured using a DC current-voltage source measure unit (KEITHLEY 2602B SYSTEM SourceMeter®) in both 2-point and 4-point configuration. This unit was also used as a constant current source (100 mA) when the Kelvin Double Bridge circuit was assembled. Using 2-point measurement, the resistance of the carbon fiber from the top voltage electrode to its corresponding bottom voltage electrode was approximately 2 Ω. Using 4-point measurement, the resistance decreased to an average of 0.5 Ω. Therefore, the total contact resistance is about 1.5 Ω. Resistor R_3 is chosen to have a similar resistance to and approximately balance the expected resistance of the carbon fiber sensor (1 Ω) to minimize the DC component of the measured voltage signal. The resistors R_1, R_2, R_1', R_2' are set to a high value (5.6 kΩ) to prevent current from flowing through them and are used for voltage measurement, thus, removing the effect of any contact and extra resistance introduced between the measurement point and the carbon fiber following the 4-point probing method.[58] The resistance of the carbon fiber device under test (R_x) can be calculated from the measured voltage V_G using formula ((4-1). The derivation of this formula can be found in Appendix B.

$$R_x = 2\frac{V_G - V_G|_{R_x=0}}{I} \tag{4-1}$$

I is the current supplied by the current source. $V_{G|(Rx=0)}$ is the measured voltage when a short circuit with zero resistance is measured instead of the carbon fiber device for calibration. Digital multiplexers are introduced to switch between electrodes and measure all possible combinations of voltage difference between the top and the bottom rows of electrodes. The multiplexers are in the voltage measurement line and have a low on-resistance compared with R_1, R_2, R_1', R_2' so that they do not affect the measurement result, just like contact resistance. The multiplexers used (ADG506AKNZ) have 16 channels, which is sufficient to study different sizes of the sensor sheet. The multiplexers were controlled using a small microcontroller (Arduino – UNO). Finally, a 12-bit DAQ unit (NI USB-6210, National Instruments) was used to measure the voltage with high accuracy and collect data in real-time. Both the microcontroller and DAQ were controlled simultaneously using a computer and programmed using MATLAB. In a future real-world implementation, both the microcontroller and the DAQ could be replaced with an application-specific integrated circuit (ASIC). The circuit was assembled using a breadboard and copper jump wires that were soldered to the printed silver contacts in the carbon fiber sheet. All circuit components used are listed in Table 4-1.

To test the damage sensor, it was connected to the circuit and measured in the undamaged state. The measurement consists of the voltage differences between each electrode from the top row of voltage electrodes and its corresponding electrode from the bottom row. Each measurement was acquired 50 times to minimize measurement error using a loop in the program, and the average of these measurements was the value used for analysis. The damage was applied by drilling holes of various sizes within the sensing area into the composite. The drill used was a SKIL 3320 10-Inch Drill with a 2 mm (5/64") drill bit at 3050 RPM. After damage was applied successively, the electrical measurements were taken again in the same manner and the mean of each set of 50 measurements was compared to its corresponding value before damage was applied.

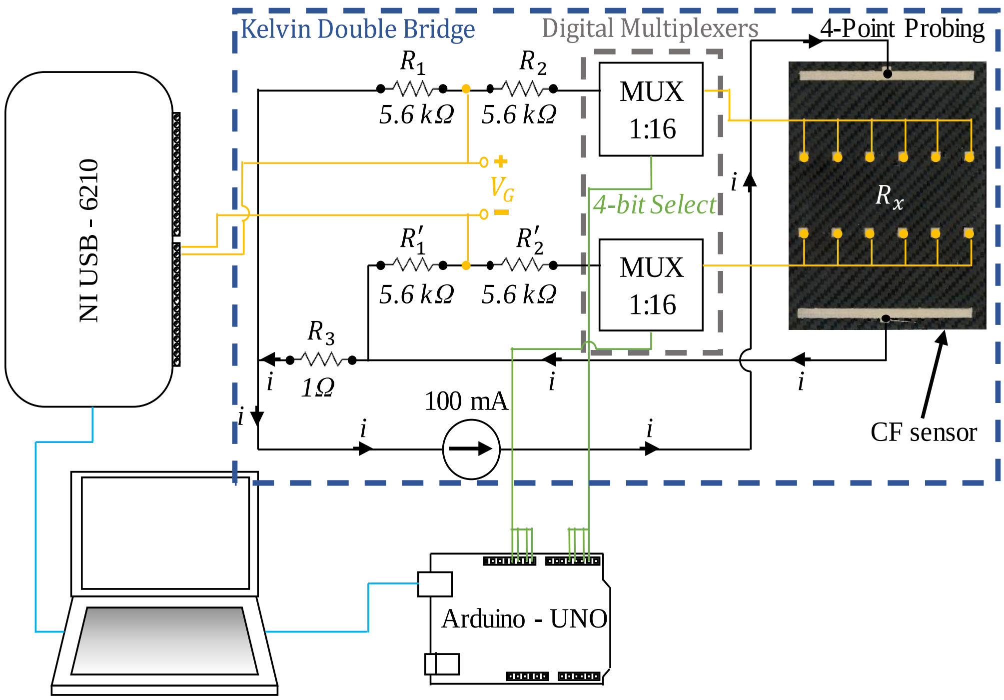

Figure 4-2. Circuit combining Kelvin Double Bridge, 4-point probing method, digital multiplexing and data acquisition tool (NI USB-6210) to automatically measure and record voltages in multiple locations on the carbon fiber (CF) sheet while canceling contact resistance

Table 4-1. List of circuit components

COMPONENT	VALUE (IF APPLICABLE)
Data Acquisition tool (NI USB-6210)	-
Arduino – UNO	-
Multiplexers (ADG506AKNZ)	-
(Current Source) KEITHLEY 2602B SYSTEM SourceMeter®	-
R_1, R_2, R'_1, R'_2	5.6 kΩ
R_3	1 Ω

4.5. Pattern Design and Simulation

The printing patterns were designed using EAGLE from Autodesk. Figure 4-3 (a) shows the dimensions of the 1-dimensional (1D) sensor where the damage could be localized only along the width of the composite. Figure 4-3 (b) shows the alteration to make the sensor detect damage in two dimensions (2D). The top and bottom bus electrodes are where the current is injected. The rows of square electrodes in the middle are used to measure the voltage across the carbon fiber sensing area. In the 2D design, the top and bottom row voltage measurements are taken relative to the middle row creating two sensing areas. Theoretically, more sensing areas could be added by adding more rows of voltage electrodes and increasing the length of the carbon fiber weave. However, this experiment was limited by the printing area of the V-One printer. Different electrode designs were analyzed qualitatively using a lumped resistor model and simulated more fully using Sentaurus 2019.03 to calculate and visualize the electric potential as a function of position in the carbon fiber sheet. Silicon doped with boron was used as the conductive material to simulate the carbon fiber weave. Changing the doping concentration of boron in silicon changes the electrical conductivity of the sheet. A high doping concentration was chosen to ensure that the silicon behaves like a conductor to simulate the carbon fiber. Silver was used to simulate the printed silver electrodes. Silicon dioxide (SiO_2), a perfect insulator, was used to simulate damage, as shown in Figure 4-3 (c). The ink used in printing has a sheet resistance one order of magnitude lower than the used carbon fiber. To match this in the simulation, the doping concentration in the silicon was chosen as 10^{22} cm^{-3} resulting in 0.39 Ω/sq sheet resistance compared with the sheet resistance of the simulation silver of 0.016 Ω/sq. However, changing the electrical conductivity of carbon fiber, silicon in the simulation, has minimal effect on the final results for the sensor when voltages are normalized as discussed below in section 4.8. This model assumes it can be neglected that the carbon fiber sheet is not a simple uniform conductor but consists of woven fiber tows.

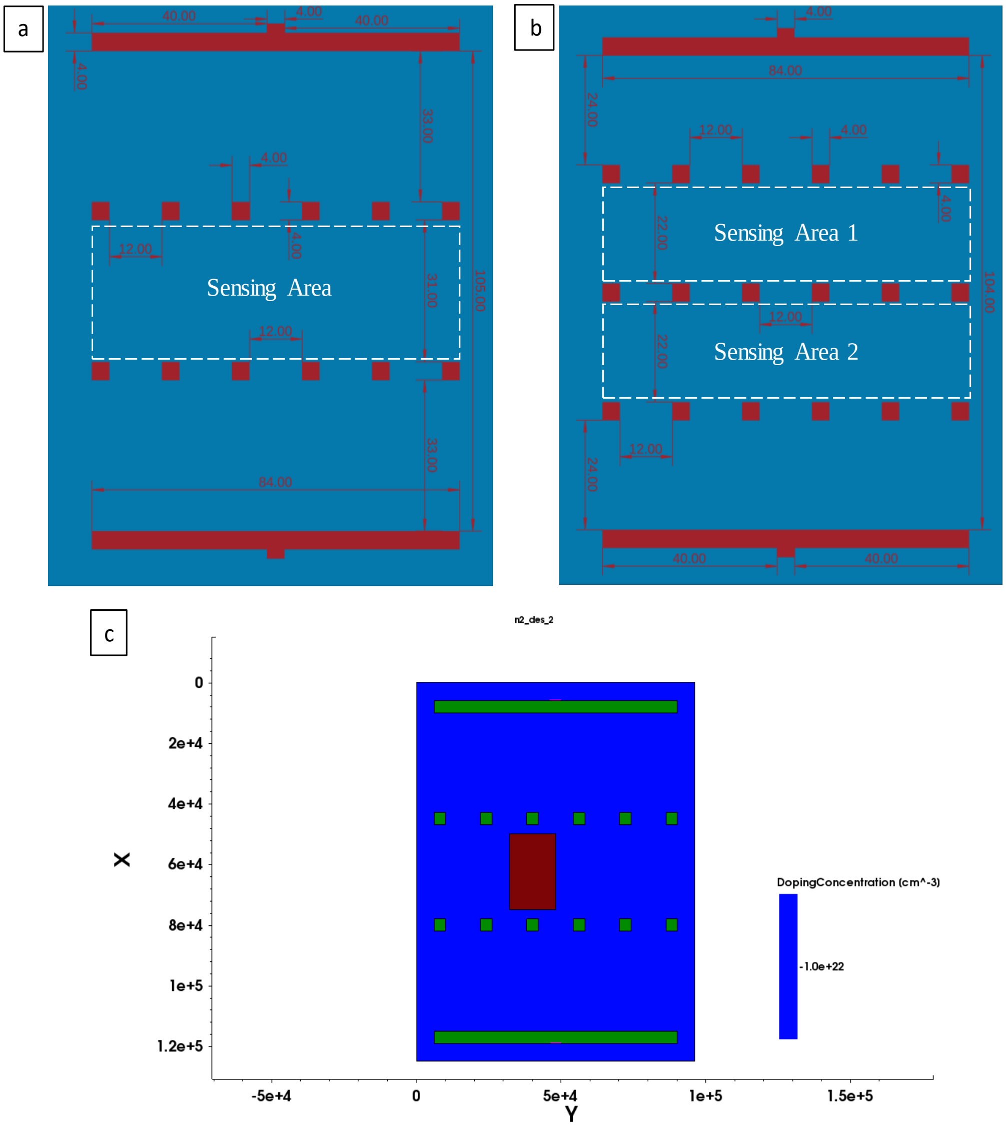

Figure 4-3. Printing pattern designs for carbon fiber damage sensors. a) EAGLE CAD design of 1D damage sensor. b) EAGLE CAD design of 2D damage sensor. Dimensions in (a) and (b) are in millimeters. c) Geometry of Sentaurus simulation of 1D damage sensor with damage introduced. Blue represents conductive carbon fiber; green represents electrodes; red represents non-conducting damage. Dimensions in (c) are in micrometers.

4.6. Lumped Resistor Model of Sensor Pattern Design

When designing the sensor pattern, the main goal is to increase the sensing area as well as spatial sensing resolution. To get a first-order understanding of the underlying physics that informs design choices, a lumped resistor model was used to model the carbon fiber sensor. This model assumes that adjacent electrodes are connected by resistors. The model ignores the distributed two-dimensional nature of conduction in the carbon fiber sheet. Therefore, it only provides qualitative, not quantitative insights; however, these insights are valuable to gain an intuitive understanding for initial design choices. Quantitative modeling is performed using finite-element modeling, as described in section 4.8.

Figure 4-4 (a) shows the circuit representation of the carbon fiber sensor sheet. The nodes at the center of the circuit correspond to the voltage electrodes of the sensor. The nodes directly connected to the current source correspond to the current bus electrodes of the sensor. The resistors represent the carbon fiber weave between the electrodes. The resistors R_{T1}, R_{T2}, R_{T3}, R_{B1}, R_{B2} and R_{B3} model the resistance between the current injection electrodes and the voltage electrodes. The resistors R_{T_1TO2}, R_{T_2TO3}, R_{B_1TO2} and R_{B_2TO3} model the resistance between the voltage electrodes. The resistors R_1, R_2 and R_3 model the main sensing area. The values of the resistors correspond to the physical distance in the pattern. The higher the resistance is, the larger the distance between the electrodes is. The current and voltage electrodes are placed very close to the current electrodes in this first design to maximize the sensing area. They are also placed close to each other. Then, the value of R_1 is increased from its value before damage (No Damage: ND) to 100 kΩ, simulating damage (D) in the area between the voltage measurement electrodes. The voltage between the current electrodes increases, which corresponds to the increased overall resistance of the carbon fiber sheet due to the damage in the weave. However, the differences in the voltage increases across R_1, R_2 and R_3 are minimal and not significant enough to be able to identify the location of the damage in the weave clearly, as shown by Design 1 in Figure 4-5 (a). This shows that this design could be used to sense the overall size of damage but not its location.

To correct this problem, the distance between the current electrodes and the voltage electrode rows is increased. This means the voltage between opposing voltage electrodes in the undamaged state is a smaller fraction of the total voltage across the weave between the current electrodes. When damage is introduced, there is more room for the measured voltage to increase. This is modeled by increasing the resistance values of R_{T1}, R_{T2}, R_{T3}, R_{B1}, R_{B2} and R_{B3} and decreasing R_1, R_2, and R_3 making all of them 0.7 Ω. Results are shown as Design 2 in Figure 4-5 (a). This shows an improved damage localization. The voltage across the damaged location 1 is now increased by 25% compared to the undamaged location 3 furthest from the damage.

To improve it further, the distance between the voltage electrodes is increased. This is modeled by increasing the resistance values of R_{T_1TO2}, R_{T_2TO3}, R_{B_1TO2} and R_{B_2TO3} to 0.2 Ω. Figure 4-4 (b) shows the final design of the damage sensor as a result of the changes from the circuit model. Results are shown as Design 3 in Figure 4-5 (a). This shows further improvement for damage localization by approximately another 30%. Figure 4-5 (b) shows the result in Figure 4-5 (a) normalized to values between 0 and 1 for the different electrodes. This normalization makes it easier to clearly pinpoint the location of the damage indicated with a value of 1.

In summary, increasing the physical distance between the current and the voltage electrodes as well as increasing the distance between the voltage electrodes in the same row increases damage localization accuracy. However, the increase in physical distance between the current electrode buses and the voltage electrode rows results in a decrease in the active sensing area. Additionally, the increase in physical distance between the voltage electrodes in the same row means that fewer electrodes could fit in the space of the carbon fiber weave, which is dictated by the application. This results in a decrease in the resolution of location-sensing as it is defined by the numbers of electrodes. Further quantification of the sensor voltage response requires a more complete consideration of the two-dimensional nature of the sheet, as shown in the following experimental results and finite-element modeling.

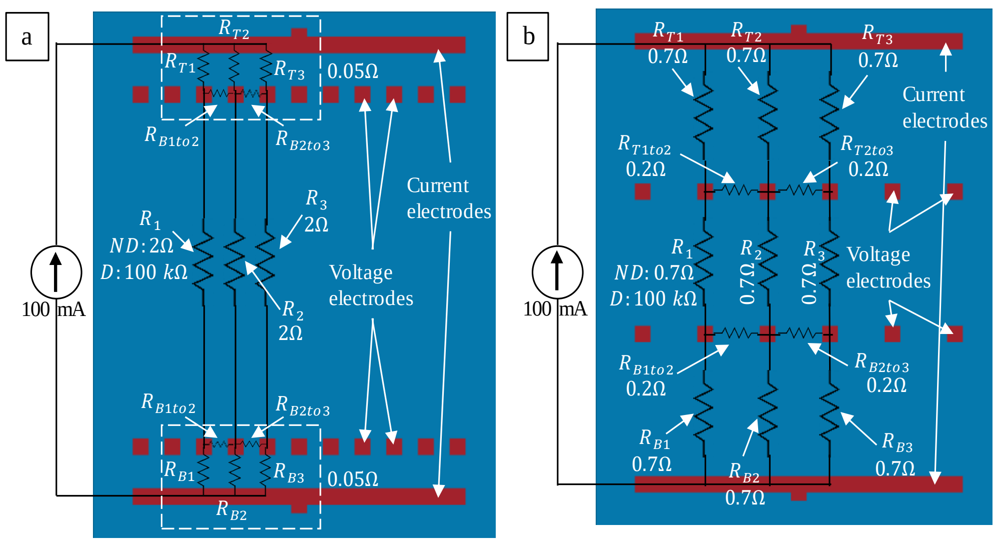

Figure 4-4. Modeling the carbon fiber damage sensor using lumped resistors. a) Design 1: Initial design and model for a damage sensor. The voltage electrodes are physically close to each other and to the current electrodes. The value of R_1 is ND: No Damage or D: with Damage. b) The final design of the damage sensor pattern with lumped resistors model.

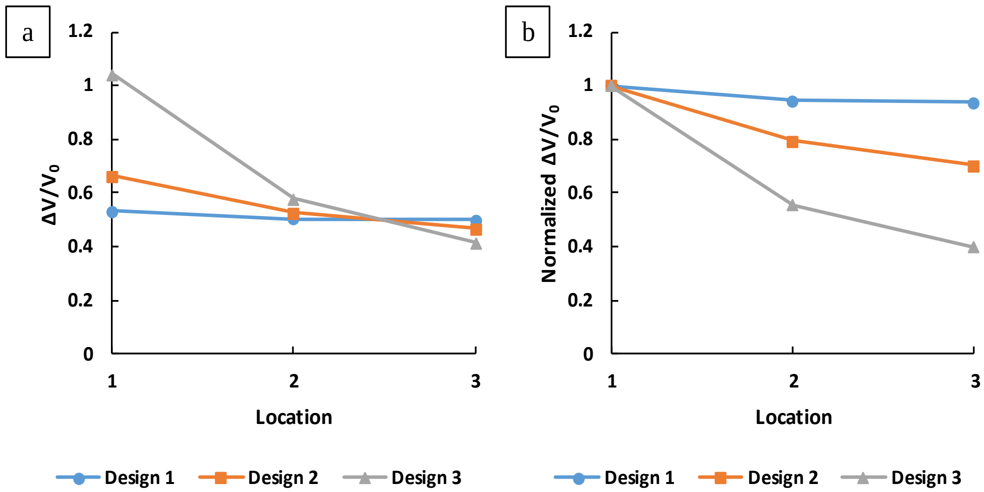

Figure 4-5. Results of modeling the carbon fiber damage sensor using lumped resistors. a) The percentage voltage change after damage in all three designs. Design 1: shown in (a), Design 2: Distance between current and voltage electrode rows increased, Design 3: Distance between voltage electrodes is also increased as shown in (c). b) The percentage voltage changes shown in (a) normalized to values between 0 and 1 for each curve for better comparison. The optimized Design 3 shows a clear difference in response between the different electrodes, which means damage location can be detected.

4.7. Testing and Electrical Measurements

The damage sensor was connected to the measurement circuit and measured before and after damage was introduced. The measurement consists of the voltage differences between the top and bottom voltage electrode pairs. The voltage electrode pairs were numbered 1 to 6, corresponding to the locations on the composite. Figure 4-6 shows the order in which damage was applied, which was rectangles of different size (I, II, III and IV) in each location and in the order of locations L3, L4, L5 and L2 consecutively. The sizes of the damage rectangles are as follows: (I): 4 mm^2; (II): 64 mm^2; (III): 128 mm^2; (IV): 288 mm^2. Figure 4-7 (a) shows the percentage increase in voltage using the average of the measurements across all locations for each damage state compared with the voltage in the undamaged state (V_0). This can be used to estimate the size of the damage applied. Due to the sensitivity and noise of the system, the smallest size damage (I) was not successfully sensed every time. The increase in damage area by 4 mm^2 increases the voltage by only 0.4% - 1.2%. The system can successfully sense and locate damage when the voltage change is above 0.7% despite of electrical noise. Damage (I) at L3, when there was no other damage present yet, increased the voltage by only 0.4%, which was too low to reliably sense its location. It is also noticed that the larger the existing damage is in the system, the more significant the newly introduced damage's effect will be on voltage because it represents a bigger relative reduction in conductive material from the remaining carbon fiber sheet. Damage size (I) was introduced to the system four times, once for each location L3, L4, L5, L2 resulting in voltage increases by 0.4%, 0.6%, 0.8% and 1.2%, respectively. Figure 4-7 (b) shows the incremental voltage change of damage size (I) for L3, L4, L5, L2 compared to the previous measurement every time a new damage is introduced. Figure 4-7 (c) shows the incremental voltage change values normalized between different electrodes to range from 0 to 1. This is used to identify the newly introduced damage location, which is supposed to have value 1. In the first measurement, the system incorrectly locates damage (I) at location 2 although it is in location 3. Conversely, the system locates damage (I) in L4, L5 and L6 successfully. The damaged location always had the largest voltage change indicated by a normalized value of 1. Damage size (II) in L3, L4, L5 and L2 increased the voltage by 0.9%, 1.4%, 2.2% and 4% respectively, making it the smallest damage that was successfully detected without any error in localizing as shown in Figure 4-7 (e).

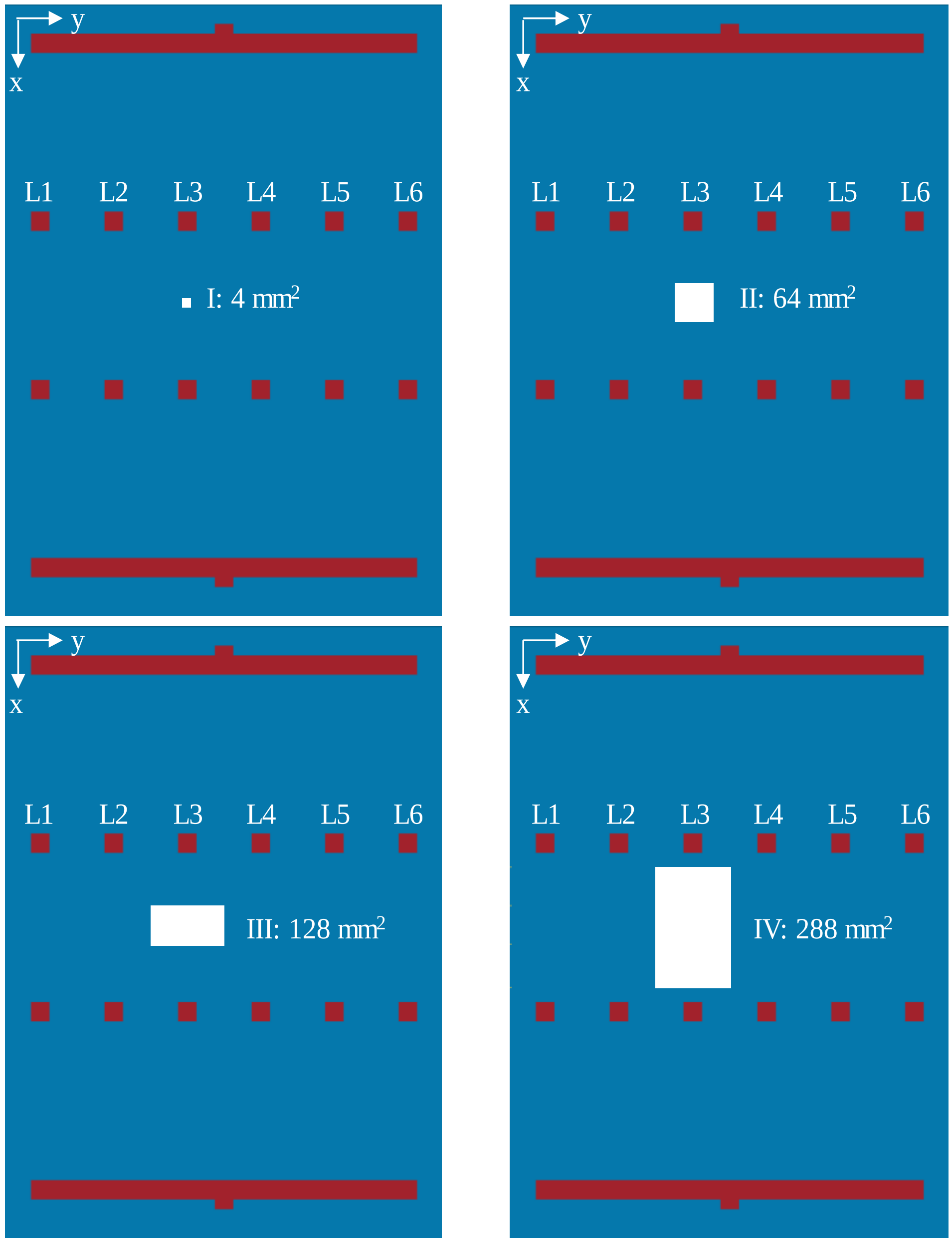

Figure 4-6. The drilling pattern in a 1D damage sensor sample proceeding from (I) to (IV) in location 3 (L3) and repeating the pattern in the same order in L4, L5 and L2 consecutively.

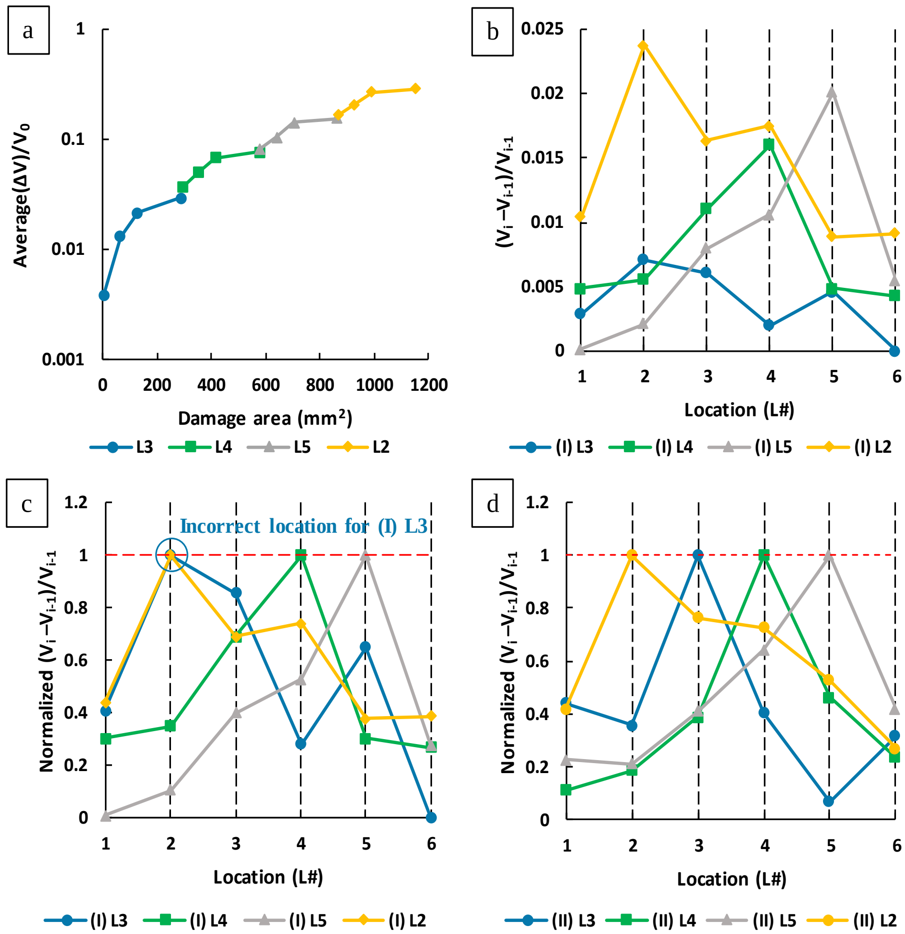

Figure 4-7. Testing 1D carbon fiber damage sensor. a) The percentage increase in voltage across the damage sensor using the average of measurements from all locations. b) Incremental voltage change between consecutive measurements for the smallest damage size (I). Subscript i-1 denotes voltage measured for previous damage state. c) Incremental voltage change for the smallest damage size (I) normalized between electrodes for each curve, showing the locations of newly introduced damage in the composite. The location with the largest voltage change has a value of 1. d) Incremental voltage change for damage size (II) normalized between electrodes of each curve, showing locations of newly introduced damage in the composite. The location with the largest voltage change has a value of 1.

Figure 4-8 shows a different sample with the same electrode geometry, but damage was applied in a different sequence. The damage was applied in increments of damage size IV (288 mm^2). The damage was drilled in the order shown in the figure from D1 to D6. Figure 4-9 (a) shows the voltage changes of the system when damage is introduced compared to the undamaged state at each location (V0). This shows how each damage introduced to the system increases the total resistance of the sensor at all locations. When D6 was drilled, the composite was divided into two completely separated parts, and the voltage measurement was limited by the voltage bounds of the current source. This is an indication that a large enough crack has occurred in the system to completely divide the sensor. To make the damage location clearer, the measured voltage changes for each damage state were normalized between 0 and 1, as shown in Figure 4-9 (b). This graph can be used to find the extent of the damage that has occurred in the composite. Any locations with a normalized voltage change of more than 70% are damaged. The same measurements were also compared to the previous measurement every time new damage was introduced to the system and normalized in the same manner, thus showing clearly with a value of 1 where the new damage was introduced, as shown in Figure 4-9 (c).

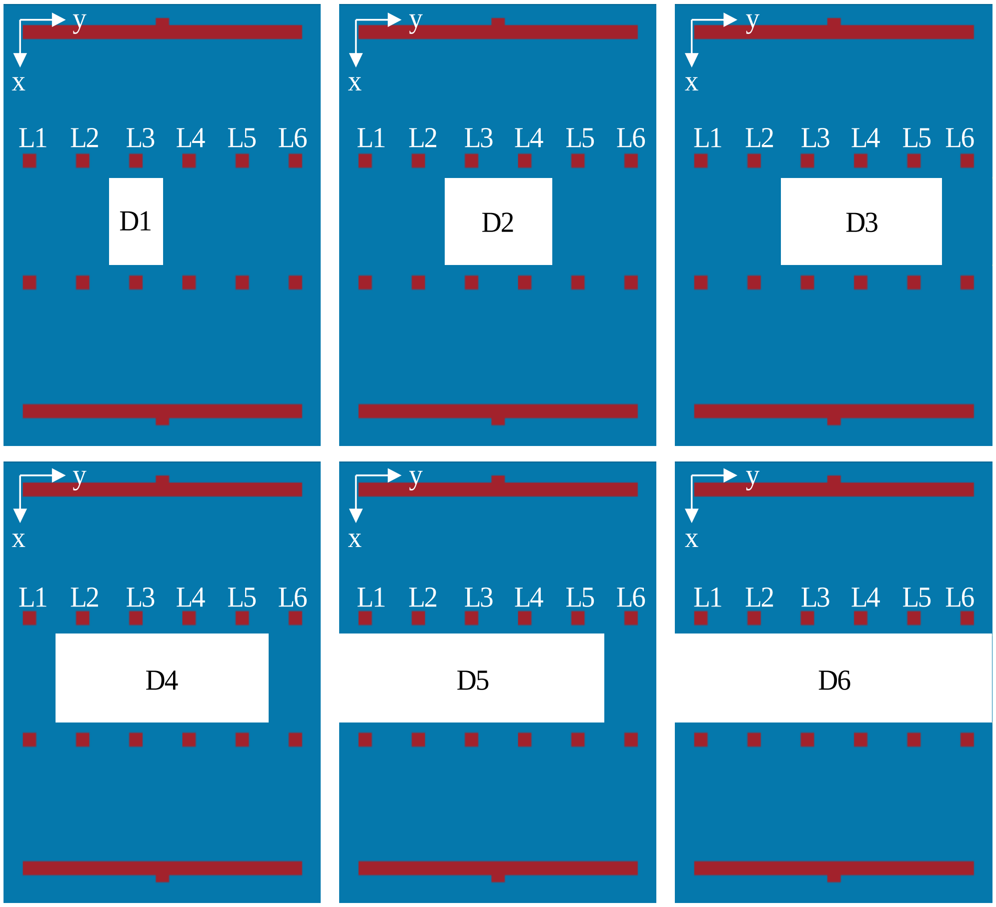

Figure 4-8. The drilling pattern in a 1D damage sensor sample progressing from D1 to D6. Damage was added cumulatively.

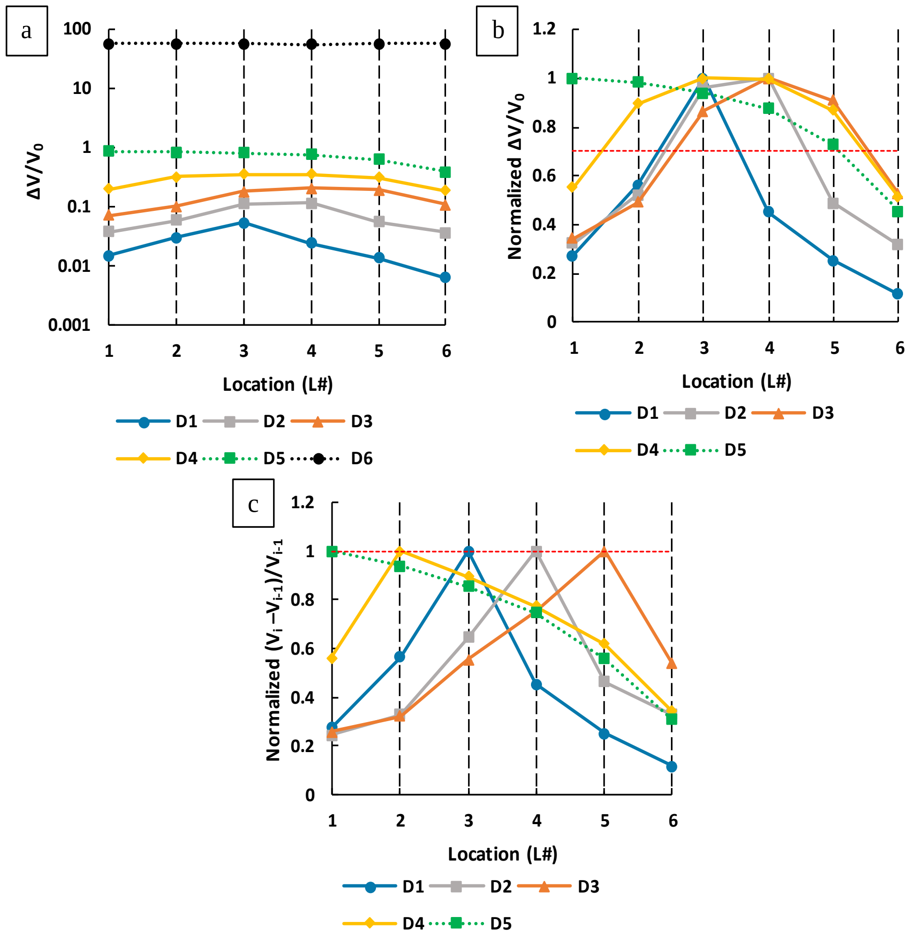

Figure 4-9. Testing 1D carbon fiber damage sensor. a) Change in voltage measurements compared to the voltage measurement at the same location before damage was introduced. The voltage increases across the entire sensor with growing damage and the largest voltage increase is found at damaged locations. b) The same data as in (a) but with voltages normalized between electrodes for each measurement curve. The locations with damage have a normalized value of 0.7 or larger (red dashed line) allowing damaged regions to be identified. c) The same data as in (b) but taking the difference between subsequent measurements. Subscript i-1 denotes voltage measured for previous damage state. The location of newly introduced damage in the composite always exhibits the biggest change normalized to 1.

For comparison, the design previously explored in section 4.6, where the voltage electrodes are closer to each other and closer to the current electrode busses (Design 1), was manufactured and tested. The design and damage drilling patterns are shown in Figure 4-10. As shown in Figure 4-11 (a), the sensor does detect damage. However, this design has a lower sensitivity compared to the design previously shown in Figure 4-6 (Design 3). The smallest damage applied to this design (Figure 4-10) was 176 mm^2, which results in a voltage change of 3.6%. Increasing the damage area to 528 mm^2 increases the voltage change by only 0.7% making the total change 4.3%. Conversely, in the previous design (Figure 4-6), a 3.7% voltage change is produced by a 292 mm^2 damage area, and increasing the damage area to 352 mm^2 increases the voltage change by 1.4%. This means that the optimized design (Figure 4-6) can resolve and sense smaller increases in damaged area. This is because the two voltage electrode rows are closer to each other and further from the current electrodes in this design as discussed in section 4.6. In addition, the design that was not optimized could not find the location of the damage at all. This is shown in Figure 4-11 (b), where the voltage change is compared to the previous state every time new damage is introduced. The data is normalized to values between 0 and 1, making the value 1 the supposed location of the newly introduced damage. When damage (D1) is introduced to the system at location 8, the sensor senses the damage at locations 1, 3, and 6 and completely misses location 8. When (D2) is applied at location 9, the damage is sensed in locations 4 and 10 and completely misses location 9. The sensor also fails to locate the damage in all other locations. This is because, in this design, the voltage electrodes are very close to each other, and the voltage electrode rows are very close to the current electrode busses. This confirms the qualitative insight gained from the lumped resistor model.

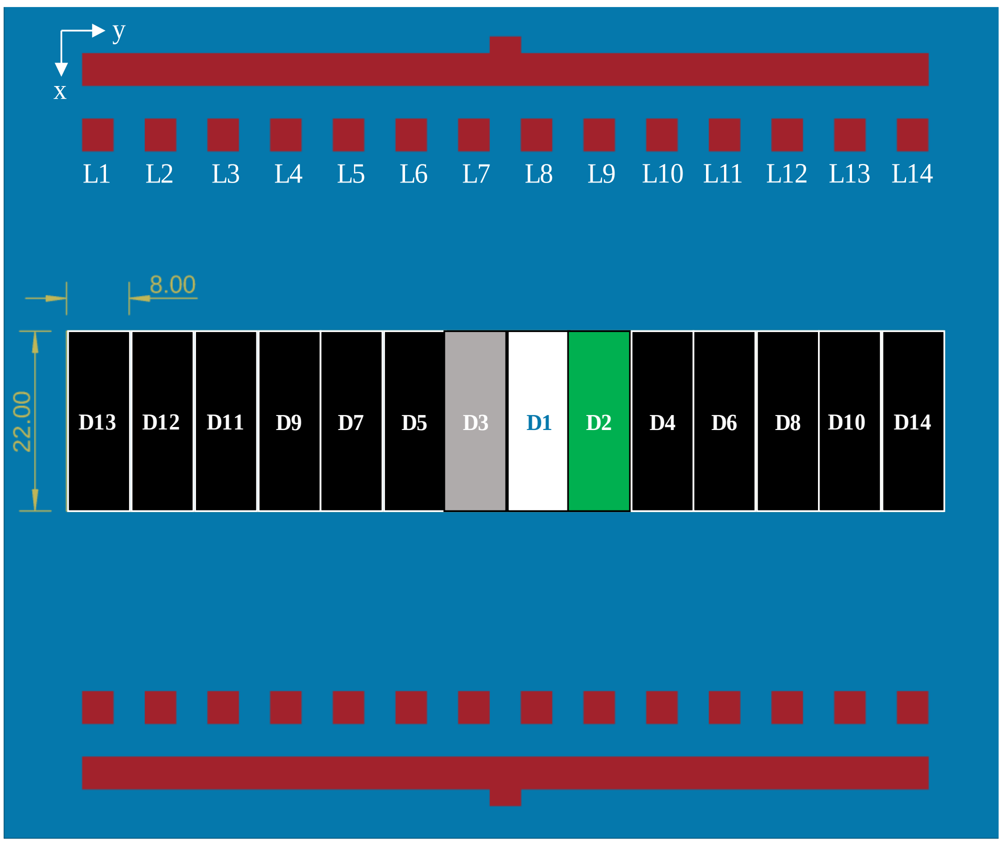

Figure 4-10. From 4.6: Design 1 where the voltage electrodes are closer to each other and closer to the current electrode busses. The drilling pattern progresses from D1 to D14. Damage was added cumulatively, e.g. D2 represents damage at locations L3 and L4. Dimensions are in millimeters.

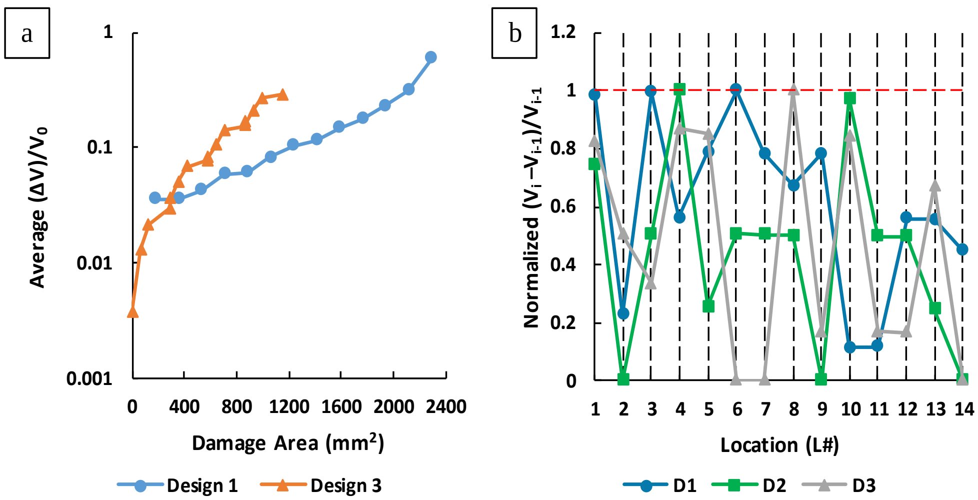

Figure 4-11. Testing 1D carbon fiber damage sensor (non-optimized Design 1). a) Percentage increase of measured voltage compared to the voltage measurement before damage was introduced, showing the increase in voltage measurements across the sensor with larger damage. Voltage is the average over all voltage measurement electrodes. Design 3: Final 1D design results included for comparison exhibit a larger sensitivity. b) Normalized percentage increase of voltage compared to the previous voltage measurement showing that the sensor fails to locate the newly introduced damage.

The same process was applied to the 2D sensor design to locate the damage in both the X- and the Y-direction. This is done by repeating the 1D pattern in multiple rows and locating the damage in each row separately. The top row sensing area was labeled L1 to L6, and the bottom row sensing area was labeled L7 to L12 both from left to right. The damage was applied in order from D1 to D6, as shown in Figure 4-12. After each damage was applied, the electrical measurements were retaken and normalized, as described previously. Figure 4-13 (a) and (b) show the normalized percentage voltage change where each measurement is compared to the previous one, thus locating newly introduced damage. This shows that damage can be sensed and located successfully in 2 dimensions.

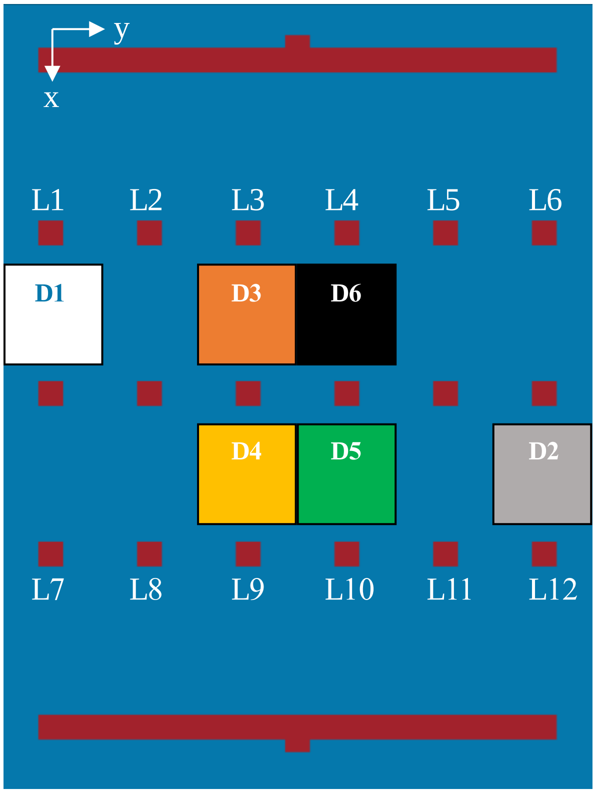

Figure 4-12. The drilling pattern in a 2D damage sensor sample progressing from D1 to D6.

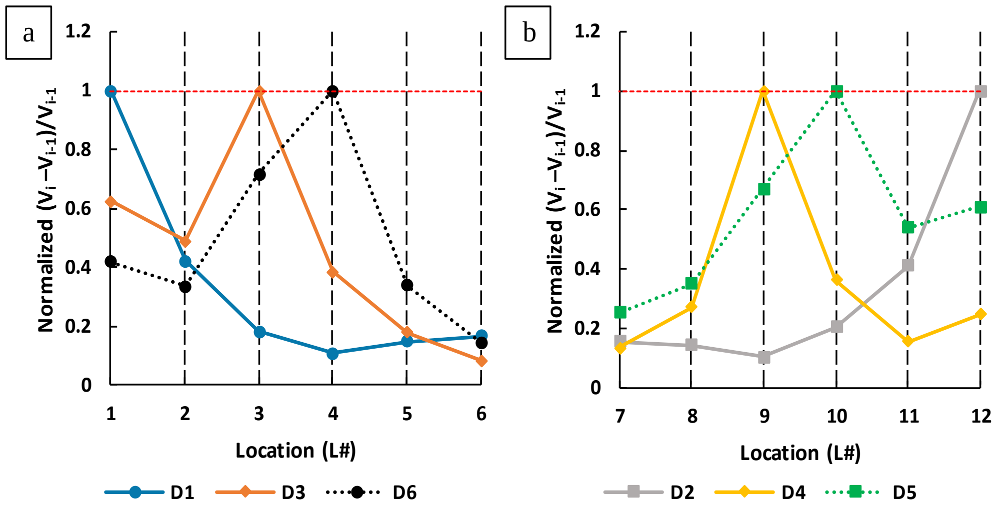

Figure 4-13. Testing 2D carbon fiber damage sensor. a) Normalized percentage voltage change in the top row compared to each previous voltage measurement (subscript i-1) showing the locations of newly introduced damage in this row. Newly created damage leads to the biggest voltage change at the corresponding location as expected (curves normalized to 1). b) The bottom row exhibits the same behavior as the top row when damage is introduced here.

4.8. Simulation Results

To validate the lumped resistor model and compare with experimental results, the damage sensor was simulated using Sentaurus 2019.03 with and without damage. Sentaurus is simulation software for silicon-based devices. The setup of this simulation is described in Appendix C. Figure 4-14 (a) shows the electrical potential as a function of position in the undamaged sheet. A voltage was applied in the middle of the current electrodes inducing current flow from top to bottom. As expected, potential drops from the top to the bottom. One can also observe current crowding around the point of current injection at the center of the electrodes since the sheet resistance of the electrodes is only one order of magnitude lower than the carbon fiber sheet. Then, damage was introduced as an electrically insulating block in the sensing area. The simulated electrical potential as a function of position is shown in Figure 4-14 (b). The electrical potential increases in the top voltage measurement electrodes where damage is introduced and decreases in the bottom electrodes. This creates an increase in the voltage difference between the top and bottom electrodes of that location, thus, increasing the resistance of the sheet in that specific area. In addition, damage in a particular location has a small effect on the neighboring locations, and its effect diminishes the farther away the electrodes are from the damage. The value of the electric potential at the electrode in front of the damage gets closer to the voltage of the closest current electrode as damage size increases until it matches it when the damage divides the sheet completely, as shown with damage D6 in Figure 4-14 (b). The increase in damage size increases the total resistance of the sheet. The resistance of the damaged sensors was compared to the non-damaged state at the different locations. It was again normalized to a range from 0 to 1 between different electrodes for each experiment as shown in Figure 4-15 (a). Comparing the plots of damage D1 and D2 from the experimental measurements and the simulation is shown in Figure 4-15 (b). It is clear that they follow the same trends and the voltage changes approximately match up. Both experiment and simulation identify the largest resistance change at the location of new damage, which is normalized to 1 in Figure 4-15 (b). Farther away from the damage location, the average discrepancy between experiment and simulation is 6%. These small differences between the trends could be due to the more complex geometry of the carbon fiber weave compared to the simulation in Sentaurus, which assumes the material is uniform, disregarding the woven nature of the carbon fiber sheet. Additional factors that may affect the experimental results include measurement errors, contact resistance, or manufacturing errors. However, by using the measurement circuit and normalizing the data as a percentage, the small differences between simulation and experiment are negligible and have no substantial effect on the performance of the sensor.

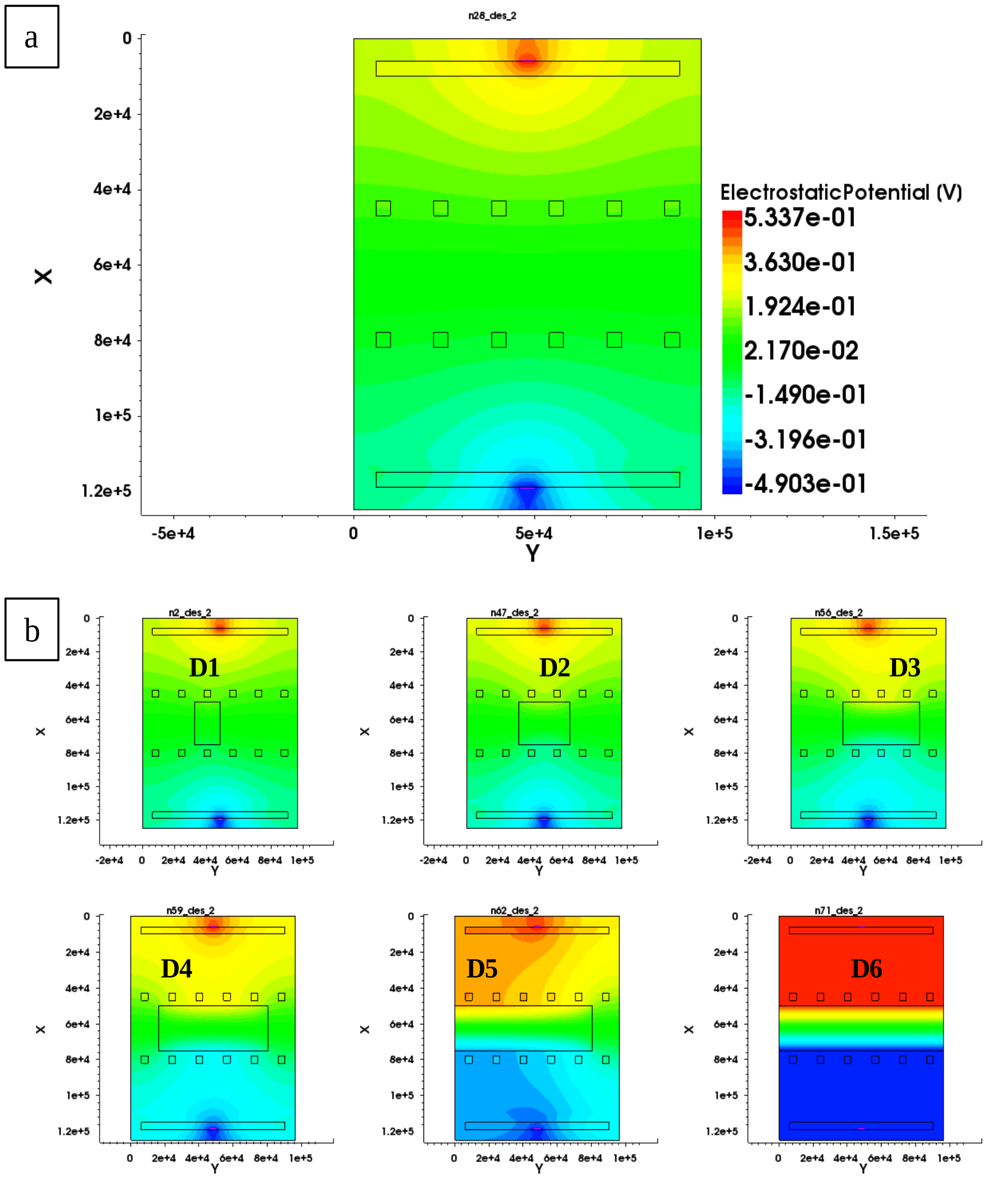

Figure 4-14. Simulation of 1D damage sensor. a) Electric potential within the undamaged carbon fiber sheet from Sentaurus simulation of 1D damage sensor. b) Sentaurus simulation of 1D damage sensor with different sizes of damage.

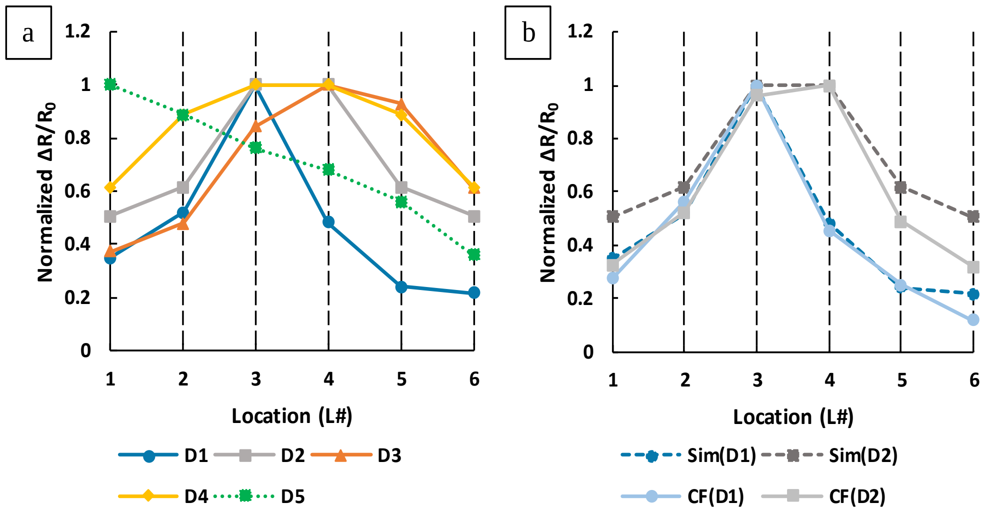

Figure 4-15. Simulation results of 1D damage sensor. a) Normalized percentage change in resistance compared to the resistance before damage was introduced. The trends are very similar to the experimental results. b) Comparison of D1 and D2 results between the simulation and the experimental (CF) results showing very good agreement.

The potential distribution in the sensor sheet depends on the relative resistance of the silver electrodes and the carbon fiber sheet. This could be different for other types of carbon fiber or silver paste. To simulate a relative decrease in carbon fiber resistance or a relative increase in silver resistance, the design was simulated using a drastically lower Boron doping in the silicon (10^{18} cm^{-3}), resulting in a resistance increase by a factor of approximately 1000 making the sheet resistance 419 Ω/sq. Results are shown in Figure 4-16 and Figure 4-17. A comparison between the two values of carbon fiber resistance shows that the potential in the high resistance sheet is distributed more evenly by the relatively less resistive current electrodes. However, when the resistance is measured with the voltage electrodes and the resistance change due to damage is normalized as before, no significant difference between the low- and high-resistance sensors is observed as shown in Figure 4-17 (b). Therefore, the damage sensor methodology presented here is likely to work with other carbon fiber and electrode material combinations as well.

These simulation results confirm the damage location mechanism based on localized voltage measurements in a conductive carbon fiber sheet. The simulated potential profiles can be used to refine designs further and decide where to place electrodes in more complex structures.

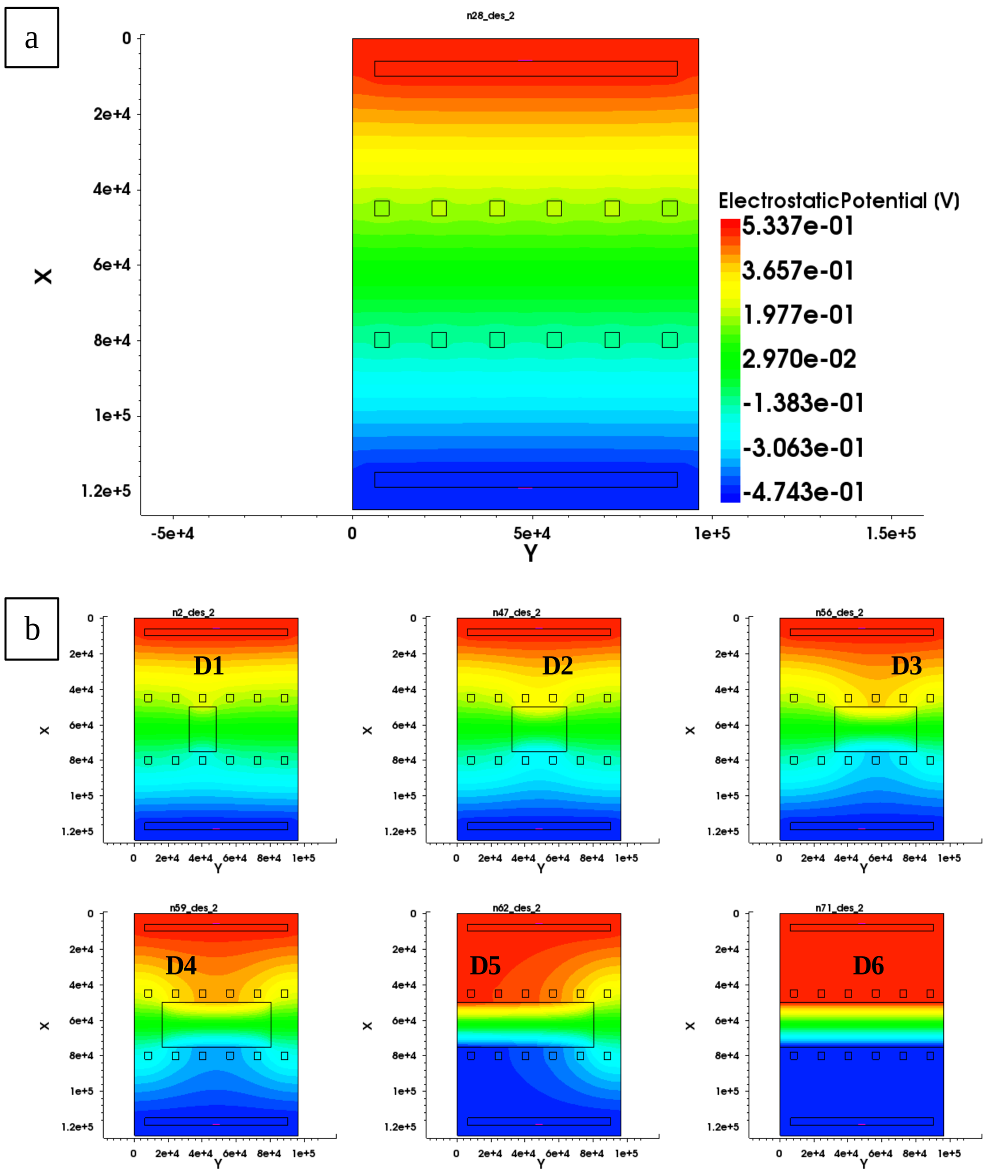

Figure 4-16. Simulation of 1D damage sensor with lower carbon fiber conductivity. a) Electric potential within the CF sheet from Sentaurus simulation of 1D damage sensor without any damage. b) Sentaurus simulation of electric potential within 1D damage sensor with different damage sizes.

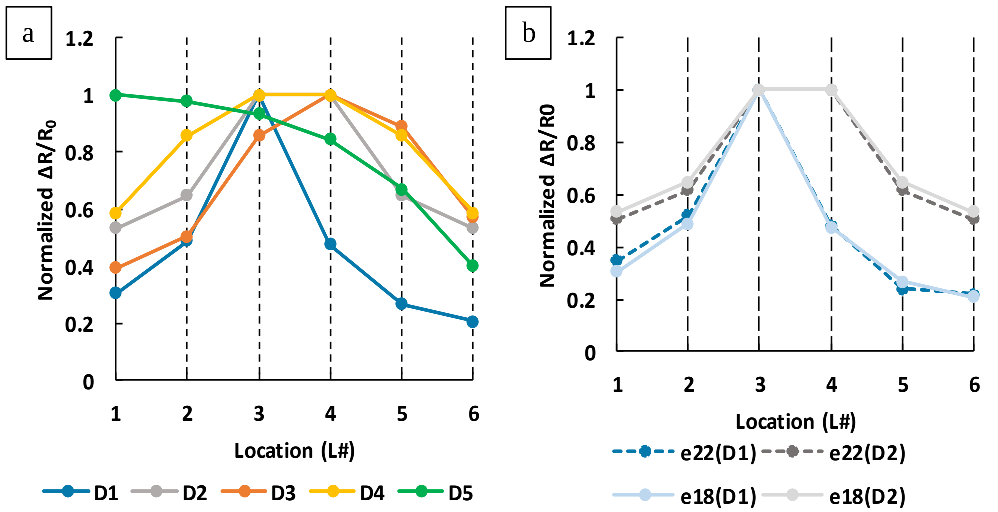

Figure 4-17. Simulation results of 1D damage sensor with lower carbon fiber conductivity. a) Normalized percentage change of resistance compared to the resistance before damage was introduced. The trends are very similar to the experimental results and simulation results with higher conductivity carbon fiber. b) Comparison of D1 and D2 results between the simulations with high (e22) and low (e18) conductivity. Results show very good agreement.

4.9. Sensor Characterization and Design Considerations

There are two different modes in which this damage sensor could potentially be used: analog or digital. In analog mode, the measured voltage values would be converted to the size of the damaged area, which could give better size resolution than the spacing of the electrodes. However, the interpretation of the measured voltage is challenging. The response is highly non-linear, as shown in Figure 4-7

(a) and Figure 4-11 (a). The voltage also depends on both x- and y-extent of the damage with different sensitivity. For example in Figure 4-7 (a), the voltage increase from damage (II) to (III) is larger than from (III) to (IV) as the sensor is more sensitive to changes in damage size in the y-direction (orthogonal to the direction of current flow) than to changes in the x-direction. Therefore, it is non-trivial to interpret measured voltage values. Further simulations or a priori knowledge of the expected damage, for example cracks in a particular direction, may make it possible to operate the sensor in analog mode. Conversely, operation in digital mode has a lower resolution but is more general.

In digital mode, each voltage electrode pair is considered as one digital sensor. All electrode pairs' voltage increases from the undamaged state are compared and normalized to values between 0 and 1. All the electrode pairs that have a value above a certain threshold (empirically identified as 0.7 here) are considered damaged. In this way, the resolution in the y-direction corresponds to the spacing between electrodes, which is 16 mm. This is the resolution both in terms of damage location and size. Damage size is estimated as the number of electrodes that show damage multiplied by their spacing. The sensor cannot reliably detect the location of 4 mm^2 sized damage but can do so for 64 mm^2 sized damage, which is therefore considered the detection threshold of the sensor in terms of damage size.

The accuracy of the sensor in digital mode is limited by its electrode spacing; hence, accuracy is ±8 mm. Accuracy could be higher in analog mode; however, this is difficult to interpret as discussed above. The two-dimensional sensor uses another set of electrodes to create a second row of measurement areas. They are evaluated digitally in the same manner to detect if there is damage in an area corresponding to an electrode pair. The resolution and accuracy is again dictated by the spacing between electrodes, now in the x-direction, which is 26 mm here. To improve the resolution, electrodes could potentially be placed closer to each other, and more rows of electrodes could be used. However, the resolution (16 mm by 26 mm) and detection threshold (64 mm^2) demonstrated here will be sufficient for many carbon fiber applications to detect damage such as bird strikes, bullet holes, or cracks. The sensor characteristics discussed above are summarized in Table 4-2. These metrics can serve as a starting point for designers when deciding whether to implement this sensing methodology in their carbon fiber composite application. There are a number of design choices and trade-offs that need to be considered, for example, total sensing area, resolution, complexity of the electronics, or smallest damage size that needs to be detected. A designer could explore this space and verify the performance of their design using the finite-element model presented here.

Table 4-2. Carbon fiber damage sensor specifications and characteristics.

	1 DIMENSIONAL SENSOR (1D)	**2 DIMENSIONAL SENSOR (2D)**
SENSING AREA DIMENSIONS	96x31 mm^2	96x22x2 mm^2
NOMINAL RESISTANCE	0.1 Ω ± 0.5 %	0.06 Ω ± 0.6 %
SENSING THRESHOLD	64 mm^2	64 mm^2
SENSING RESOLUTION	16 mm on y-axis	16 mm on y-axis; 26 mm on x-axis
REFERENCE TEMPERATURE	23 °C	23 °C

4.10. Conclusions

This chapter presents a 2D digital damage sensing method for woven carbon fiber composites using printed electronics. Conventional composite manufacturing techniques are integrated with the addition of printing electronics on carbon fiber weaves using extrusion printing. Damage is detected by injecting current into the conductive carbon fiber from printed electrodes and measuring voltage at strategic locations with another set of printed electrodes. A circuit that automates switching between electrodes to take high-accuracy measurements and remove contact resistance was designed using a combination of the Kelvin Double Bridge, 4-point probing method, digital multiplexers, and a data acquisition unit. This circuit allows for the scaling of the sensor by merely adding more channels to the multiplexers, thus, enabling the expansion of the sensing area and the increase of spatial resolution as needed. The sensor can successfully detect the size and location of damage. Its resolution is limited by the spacing of the electrodes, which is 16 mm in the y-direction (orthogonal to current flow) and 26 mm in the x-direction. The threshold size of damage that can be detected is 64 mm^2. Different pattern designs were studied experimentally, qualitatively modeled using a lumped resistor model, and simulated using finite-element modeling. The simulation results match the measurement trends with an average difference of 6%. These simulations could be used by designers to adapt the method to the size and shape of their carbon fiber composite application. Further improvements in resolution may also be possible with further optimization; however, the resolution demonstrated here will be sufficient for many applications to detect damage such as bird strikes, bullet holes, or cracks. The resulting damage sensing carbon fiber composite could be integrated into the manufacturing process of composite structures as one of the layers or added to surfaces of existing large-area structures enabling smart structures and structural health monitoring.

CHAPTER 5. CONCLUSION AND FUTURE WORK

In this chapter, the conclusions from this thesis are summarized. Then, suggestions are made for future work that could build specifically on the results of this thesis.

5.1. Conclusions

The main goal and contribution of this thesis is to use extrusion printing to print electronics on woven carbon fiber exploiting the conductive nature of carbon fiber and, as a consequence, create two new electronic devices. First, a self-heating carbon fiber composite that could be integrated in various structures including UAVs. Second, a damage sensor that senses and locates holes in two dimensions.

In chapter 2, a novel approach to using extrusion printing to print on textile composites, specifically, carbon fiber weaves is demonstrated. The large surface roughness of textiles is the main challenge for extrusion printing electronics on these textiles. This challenge was overcome by increasing the standoff distance between the nozzle and the textile. To nevertheless achieve good print quality and sufficient ink flow, the piston pressure inside the ink cartridge was increased whilst compensating for the loss in pressure throughout a print run. As a result, the manufacturing of the carbon fiber-based devices is repeatable and scalable. Moreover, extrusion printing is a contactless digital printing method, thus it allows for the facile variation of the pattern design to create various types of electronic devices and circuits.

In chapter 3, the manufacturing process of a carbon fiber composite heating device is demonstrated. This device could be integrated into UAVs for de-icing. The manufacturing of the integrated heating devices is based on commonly used composites manufacturing methods with the addition of a printing step to create electrical contacts. Using an IR camera, temperature measurements of the manufactured devices were taken, and results show that the fabricated devices can achieve high temperatures suitable for melting ice on UAVs. The devices were fabricated using three different carbon fiber weaves (3K Twill, 6K Twill and 12K Unidirectional). The 3K and 6K Twill weaves are preferred for this integrated heater because they show similar behavior where the heat spreads uniformly over the area between the two electrodes. In contrast, in the 12K Unidirectional weave the heat generated along the tows spreads less to the adjacent tows.

In chapter 4, a 2D digital damage sensor for woven carbon fiber composites using printed electronics is presented. The manufacturing process of this sensor is also based on conventional composite manufacturing techniques with the addition of printing electronics on carbon fiber weaves using extrusion printing. The resulting damage sensing carbon fiber composite could be integrated into the manufacturing process of composite structures as one of the layers or added to surfaces of existing large-area structures enabling smart structures and structural health monitoring. To detect damage, current is injected into the conductive carbon fiber from printed electrodes and voltage is measured at strategic locations with another set of printed electrodes. To automate switching between electrodes, take high-accuracy measurements, and remove contact resistance, a read-out circuit was designed. This circuit combines the Kelvin Double Bridge, 4-point probing method, digital multiplexers, and a data acquisition unit. This circuit potentially enables the expansion of the sensing area and the increase of spatial resolution as needed. The scaling of the sensor could be done by merely adding more channels to the multiplexers. The sensor can successfully detect the size and location of damage. The threshold size of damage that can be detected is 64 mm^2. Its resolution is limited by the spacing of the electrodes, which is 16 mm in the y-direction (orthogonal to current flow) and 26 mm in the x-direction. Different pattern designs were studied experimentally, qualitatively modeled using a lumped resistor model, and simulated using finite-element modeling. The simulation results match the measurement trends with an average difference of 6%. These simulations could be used by designers to adapt the method to the size and shape of their carbon fiber composite application. The resolution demonstrated here will be sufficient for many applications to detect damage such as bird strikes, bullet holes, or cracks.

5.2. Future work

There are a number of ways to build on the success of extrusion printing on textiles and creating the carbon fiber heater and damage sensor. In this thesis, extrusion printing on textiles was limited by two factors. The small printing area and the printer's closed source software. Increasing the printing area will allow scaling the devices to larger areas. This will allow increasing the heating area in the heater. As for the damage sensor, it will allow for the increase of sensing area by adding more electrodes. The closed source software limited the control over the printing order of the lines. Controlling printing order would enable the optimization and improvement of the quality of printed features. In addition, although the software permitted the optimization of some printing parameters, it was still limited by the upper and lower bounds and increments of parameters set by the printer manufacturer. These issues could be solved by using alternative commercial printers or building an easily customizable printer. Furthermore, these printing methods could be tested and optimized with textiles other than woven carbon fiber that could potentially present new challenges.

The demonstrated proof of concept devices have room for improving the devices in multiple ways. First, in this thesis, optimizing the main printing parameters was tackled, but the printer offers more parameters that could, if optimized, potentially improve the quality of printed features. Second, the silver ink used for printing was an order of magnitude less conductive than bulk silver.

Using a more conductive silver ink will increase (*P(L)*%) of the heater and enable designing wider area heaters. Third, the manufacturing methods used in this thesis often resulted in air bubbles trapped in the epoxy. These air bubbles had no effect on the (*P(L)*%) of the devices but they have an effect on the mechanical integrity of the carbon fiber composites. This issue could potentially be solved by introducing vacuum bags in the epoxy curing manufacturing step. Fourth, in this thesis, the epoxy covering the silver electrodes was burnt away manually using a soldering iron. This process is time consuming and has unstable results. The process could be automated and optimized. Fifth, after the epoxy is burnt off, copper jump wires were soldered to the silver electrodes to inject current in the carbon fiber composite or connect to the rest of the circuit. However, the epoxy has a smooth finish, thus, the wires could be replaced by printing them and mounting any circuit components directly on the composites itself. This will eliminate noise created by the jump wires and create an integrated device. Finally, the circuit used for measuring the damage sensor included elements for the Kelvin Double Bridge, digital multiplexers, an Arduino microprocessor to control the multiplexers and a data acquisition unit. All these parts could be combined by designing one application specific integrated circuit (ASIC). In addition, with future advancements in printed electronics technologies, this ASIC could potentially be fully printed on the carbon fiber composite, thus, decreasing the complexity and price of manufacturing the integrated carbon fiber damage sensor.

In this thesis, the devices' design optimization processes were studied and discussed. However, the fabricated devices were not at the full potential of possible optimization. As discussed in chapter 3, the heater device (*P(L)*%) could be increased by increasing the physical length of the device which, as previously discussed, was not possible due to the limited printing area. The damage sensor design, on the other hand, has many opportunities for studies and improvement. First, the sensor in chapter 4 was manufactured using only one type of carbon fiber weave. Different types of weaves and braids could potentially have an effect on the resolution and accuracy of the sensor. In addition, carbon fibers could be woven together with other materials. These materials could have a different electrical conductivity from carbon fiber or could be insulating. In such cases, the orientation of the fibers might have a larger effect on the measurement results. Similar material, such as graphene and carbon nanotubes, could also be used instead of carbon fiber and compared to improve the sensor. Second, the number of electrodes is limited by the available printing area; however, if the electrodes were physically moved closer to each other more electrodes could be added. This presents a tradeoff between the resolution of sensing and possible number of sensing locations. The design process of the damage sensor could be used to optimize this tradeoff according to desired application. Finally, the carbon fiber weave used for the damage sensor was a (2x2) Twill weave so the electrode sizes were designed to, ideally, be in contact with the smallest cell defined as a square of 2x2 tows.

However, the size of the electrodes could be optimized to potentially increase the number of sensing locations, sensor resolution, sensor accuracy and the threshold of damages size that is possible sense.

In conclusion, this thesis has presented a method of using extrusion printing with carbon fiber composites to create electronic devices. This paves the way for future research in multiple topics. These topics include improving and optimizing printing on textiles, improving and optimizing the presented heater device and damage sensor to be used in commercial applications, and, finally, using the proposed methods to innovate and invent more large-area electronic devices for various applications.

BIBLIOGRAPHY

[1] J. S. Chang, A. F. Facchetti, and R. Reuss, “A Circuits and Systems Perspective of Organic/Printed Electronics: Review, Challenges, and Contemporary and Emerging Design Approaches,” *IEEE J. Emerg. Sel. Top. Circuits Syst.*, vol. 7, no. 1, pp. 7–26, Mar. 2017.

[2] Y. Khan, A. Thielens, S. Muin, J. Ting, C. Baumbauer, and A. C. Arias, “A New Frontier of Printed Electronics: Flexible Hybrid Electronics,” *Adv. Mater.*, p. 1905279, Nov. 2019.

[3] H. F. Castro *et al.*, “Degradation of all-inkjet-printed organic thin-film transistors with TIPS-pentacene under processes applied in textile manufacturing,” *Org. Electron.*, vol. 22, pp. 12–19, Jul. 2015.

[4] M. Stoppa and A. Chiolerio, “Wearable electronics and smart textiles: A critical review,” *Sensors (Switzerland)*, vol. 14, no. 7. pp. 11957–11992, 07-Jul-2014.

[5] I. Kazani, C. Hertleer, G. de Mey, A. Schwarz, G. Guxho, and L. van Langenhove, “Electrical conductive textiles obtained by screen printing,” *Fibres Text. East. Eur.*, vol. 90, no. 1, pp. 57–63, 2012.

[6] A. E. Ostfeld, I. Deckman, A. M. Gaikwad, C. M. Lochner, and A. C. Arias, “Screen printed passive components for flexible power electronics,” *Sci. Rep.*, vol. 5, Oct. 2015.

[7] Y. Li, R. Torah, S. Beeby, and J. Tudor, “An all-inkjet printed flexible capacitor on a textile using a new poly(4-vinylphenol) dielectric ink for wearable applications,” in *Proceedings of IEEE Sensors*, 2012, pp. 1–4.

[8] W. Tang *et al.*, “Recent progress in printable organic field effect

transistors," *Journal of Materials Chemistry C*, vol. 7, no. 4. Royal Society of Chemistry, pp. 790–808, 2019.

[9] Z. Stempien, E. Rybicki, T. Rybicki, and J. Lesnikowski, "Inkjet-printing deposition of silver electro-conductive layers on textile substrates at low sintering temperature by using an aqueous silver ions-containing ink for textronic applications," *Sensors Actuators B Chem.*, vol. 224, pp. 714–725, Mar. 2016.

[10] K. B. Perez and C. B. Williams, "Combining additive manufacturing and direct write for integrated electronics - A review," in *24th International SFF Symposium - An Additive Manufacturing Conference, SFF 2013*, 2013, pp. 962–979.

[11] K. Suganuma, "Printing Technology," 2014, pp. 23–48.

[12] M. G. Mohammed and R. Kramer, "All-Printed Flexible and Stretchable Electronics," *Adv. Mater.*, vol. 29, no. 19, May 2017.

[13] P. Bhatt and A. Goe, "Carbon Fibres: Production, Properties and Potential Use," *Mater. Sci. Res. India*, vol. 14, no. 1, pp. 52–57, Jun. 2017.

[14] M. S. Scholz *et al.*, "The use of composite materials in modern orthopaedic medicine and prosthetic devices: A review," *Composites Science and Technology*, vol. 71, no. 16. Elsevier, pp. 1791–1803, 14-Nov-2011.

[15] B. A. Newcomb, "Processing, structure, and properties of carbon fibers," *Composites Part A: Applied Science and Manufacturing*, vol. 91. Elsevier Ltd, pp. 262–282, 01-Dec-2016.

[16] X. Huang, "Fabrication and properties of carbon fibers," *Materials*, vol. 2, no. 4. pp. 2369–2403, 2009.

[17] G. Grau, E. J. Frazier, and V. Subramanian, "Printed unmanned aerial vehicles using paper-based electroactive polymer actuators and organic ion gel transistors," *Microsystems Nanoeng.*, vol. 2, 2016.

[18] M. Ader and D. Axelsson, "Drones in arctic environments," 2017.

[19] R. W. Gent, N. P. Dart, and J. T. Cansdale, "Aircraft icing," *Philos. Trans. R. Soc. A Math. Phys. Eng. Sci.*, vol. 358, no. 1776, pp. 2873–2911, 2000.

[20] A. Beisswenger, C. Laforte, and J. Perron, "Issues and testing of non-glycol aircraft ground deicing fluids," in *SAE Technical Papers*, 2011.

[21] K. L. Sørensen, *Autonomous Icing Protection Solution for Small Unmanned Aircraft: An Icing Detection, Anti-Icing and De-Icing Solution*. 2016.

[22] Y. Ibrahim, R. Kempers, and A. Amirfazli, "3D printed electro-thermal anti- or de-icing system for composite panels," *Cold Reg. Sci. Technol.*, vol. 166, p. 102844, Oct. 2019.

[23] C. Ferro, R. Grassi, C. Seclì, and P. Maggiore, "Additive Manufacturing Offers New Opportunities in UAV Research," in *Procedia CIRP*, 2016.

[24] S. Morton, R. D'Sa, and N. Papanikolopoulos, "Solar powered UAV: Design and experiments," in *IEEE International Conference on Intelligent Robots and Systems*, 2015, vol. 2015-December, pp. 2460–2466.

[25] X. Yao, S. C. Hawkins, and B. G. Falzon, "An advanced anti-icing/de-icing system utilizing highly aligned carbon nanotube webs," *Carbon N. Y.*, vol. 136, pp. 130–138, Sep. 2018.

[26] L. Vertuccio, F. De Santis, R. Pantani, K. Lafdi, and L. Guadagno, "Effective de-icing skin using graphene-based flexible heater," *Compos.*

Part B Eng., vol. 162, pp. 600–610, Apr. 2019.

[27] Y. Ming, Y. Duan, S. Zhang, Y. Zhu, and B. Wang, "Self-heating 3D printed continuous carbon fiber/epoxy mesh and its application in wind turbine deicing," *Polym. Test.*, vol. 82, Feb. 2020.

[28] O. Galao, L. Bañón, F. Baeza, J. Carmona, and P. Garcés, "Highly Conductive Carbon Fiber Reinforced Concrete for Icing Prevention and Curing," *Materials (Basel).*, vol. 9, no. 4, p. 281, Apr. 2016.

[29] H. Zhao, Z. Wu, S. Wang, J. Zheng, and G. Che, "Concrete pavement deicing with carbon fiber heating wires," *Cold Reg. Sci. Technol.*, vol. 65, no. 3, pp. 413–420, Mar. 2011.

[30] D. Zhao, T. Liu, M. Zhang, R. Liang, and B. Wang, "Fabrication and characterization of aerosol-jet printed strain sensors for multifunctional composite structures," *Smart Mater. Struct.*, vol. 21, no. 11, Nov. 2012.

[31] T. Augustin, "Structural health monitoring of carbon fiber reinforced polymers and carbon nanotube modified adhesive joints via electrical resistance measurement," pp. 1–127, 2018.

[32] T. Augustin, D. Grunert, H. H. Langner, V. Haverkamp, and B. Fiedler, "Online monitoring of surface cracks and delaminations in carbon fiber/epoxy composites using silver nanoparticle based ink," *Adv. Manuf. Polym. Compos. Sci.*, vol. 3, no. 3, pp. 110–119, Jul. 2017.

[33] F. Heinrich and R. Lammering, "A numerical approach to simulate printed electronics on fiber reinforced composites," *PAMM*, vol. 16, no. 1, pp. 135–136, Oct. 2016.

[34] F. Heinrich and R. Lammering, "An experimental investigation on the adhesion of printed electronics on fiber reinforced composites," in *8th*

European Workshop on Structural Health Monitoring, EWSHM 2016, 2016, vol. 4, pp. 2949–2956.

[35] F. Heinrich, T. Genco, and R. Lammering, “On the mechanical behavior of a composite stiffener with inkjet-printed electronics,” in *9th European Workshop on Structural Health Monitoring, EWSHM 2018*, 2018.

[36] A. Schiavone, I. T. Garces, G. W. Melenka, and C. Ayranci, “Achieving Structural Health Monitoring Using Additive Manufacturing,” *Des. Manuf. Appl. Compos. - Twelfth Jt. Canada-Japan Work. Compos.*, 2018.

[37] Y. Lingyu and V. Giurgiutiu, “Multi-mode damage detection methods with piezoelectric wafer active sensors,” *J. Intell. Mater. Syst. Struct.*, vol. 20, no. 11, pp. 1329–1341, Jul. 2009.

[38] C. R. Farrar and K. Worden, “An introduction to structural health monitoring,” *Philos. Trans. R. Soc. A Math. Phys. Eng. Sci.*, vol. 365, no. 1851, pp. 303–315, Feb. 2007.

[39] C. R. Farrar and N. A. J. Lieven, “Damage prognosis: The future of structural health monitoring,” *Philos. Trans. R. Soc. A Math. Phys. Eng. Sci.*, vol. 365, no. 1851, pp. 623–632, Feb. 2007.

[40] Z. Wan, J. D. Li, M. Jia, and J. L. Li, “Structural health monitoring (SHM) of three-dimensional braided composite material using carbon nanotube thread sensors,” *J. Mech.*, vol. 29, no. 4, pp. 617–621, 2013.

[41] J. M. Ko and Y. Q. Ni, “Technology developments in structural health monitoring of large-scale bridges,” *Eng. Struct.*, vol. 27, no. 12 SPEC. ISS., pp. 1715–1725, Oct. 2005.

[42] A. C. Douglass and J. B. Harley, “Model-based statistical guided wave damage detection for an aluminum plate,” *Struct. Heal. Monit.*, p.

147592172090950, Mar. 2020.

[43] A. N. Zagrai and V. Giurgiutiu, "Electro-Mechanical Impedance Method for Crack Detection in Thin Plates," *J. Intell. Mater. Syst. Struct.*, vol. 12, no. 10, pp. 709–718, Oct. 2001.

[44] V. Giurgiutiu, A. Zagrai, and J. Bao, "Damage identification in aging aircraft structures with piezoelectric wafer active sensors," in *Journal of Intelligent Material Systems and Structures*, 2004, vol. 15, no. 9–10, pp. 673–687.

[45] I. Perez-Alfaro, D. Gil-Hernandez, O. Muñoz-Navascues, J. Casbas-Gimenez, J. C. Sanchez-Catalan, and N. Murillo, "Low-cost piezoelectric sensors for time domain load monitoring of metallic structures during operational and maintenance processes," *Sensors (Switzerland)*, vol. 20, no. 5, Mar. 2020.

[46] I. Jerkovic, V. Koncar, and A. Grancaric, "New Textile Sensors for In Situ Structural Health Monitoring of Textile Reinforced Thermoplastic Composites Based on the Conductive Poly(3,4-ethylenedioxythiophene)-poly(styrenesulfonate) Polymer Complex," *Sensors*, vol. 17, no. 10, p. 2297, Oct. 2017.

[47] X. Fu and D. D. L. Chung, "Self-monitoring of fatigue damage in carbon fiber reinforced cement," *Cem. Concr. Res.*, vol. 26, no. 1, pp. 15–20, Jan. 1996.

[48] X. Wang, S. Wang, and D. D. L. Chung, "Sensing damage in carbon fiber and its polymer-matrix and carbon-matrix composites by electrical resistance measurement," *J. Mater. Sci.*, vol. 34, no. 11, pp. 2703–2713, 1999.

[49] S. Wen and D. D. L. Chung, “Electrical-resistance-based damage self-sensing in carbon fiber reinforced cement,” *Carbon N. Y.*, vol. 45, no. 4, pp. 710–716, Apr. 2007.

[50] S. Wang and D. D. L. Chung, “Self-sensing of flexural strain and damage in carbon fiber polymer-matrix composite by electrical resistance measurement,” *Carbon N. Y.*, vol. 44, no. 13, pp. 2739–2751, Nov. 2006.

[51] L. Gao, E. T. Thostenson, Z. Zhang, and T. W. Chou, “Sensing of damage mechanisms in fiber-reinforced composites under cyclic loading using carbon nanotubes,” *Adv. Funct. Mater.*, vol. 19, no. 1, pp. 123–130, Jan. 2009.

[52] Y. Okabe, N. Tanaka, and N. Takeda, “Effect of fiber coating on crack detection in carbon fiber reinforced plastic composites using fiber Bragg grating sensors,” *Smart Mater. Struct.*, vol. 11, no. 6, p. 892, Oct. 2002.

[53] L. Cheng and G. Y. Tian, “Surface crack detection for carbon fiber reinforced plastic (CFRP) materials using pulsed eddy current thermography,” *IEEE Sens. J.*, vol. 11, no. 12, pp. 3261–3268, 2011.

[54] Y. Okabe, S. Yashiro, T. Kosaka, and N. Takeda, “Detection of transverse cracks in CFRP composites using embedded fiber Bragg grating sensors,” *Smart Mater. Struct.*, vol. 9, no. 6, p. 832, 2000.

[55] C. Cherif, E. Haentzsche, R. Mueller, A. Nocke, M. Huebner, and M. M. B. Hasan, “Carbon fibre sensors embedded in glass fibre-based composites for windmill blades,” *Smart Text. Their Appl.*, pp. 329–352, 2016.

[56] J. Qiu, M. K. Idris, G. Grau, and G. W. Melenka, “Fabrication of electroluminescent carbon fiber composite for damage visualization,” *Manuf. Lett.*, vol. 24, pp. 56–60, Apr. 2020.

[57] M. S. Rahman and G. Grau, "Direct writing of stretchable metal flake conductors: improved stretchability and conductivity by combining differently sintered materials," *Flex. Print. Electron.*, vol. 5, no. 2, p. 025005, Jun. 2020.

[58] C. Jooss *et al.*, "The 100th anniversary of the four-point probe technique: The role of probe geometries in isotropic and anisotropic systems," *J. Phys. Condens. Matter*, vol. 27, no. 22, p. 223201, 2015.

[59] A. Horoschenkoff and C. Christner, "Carbon Fibre Sensor : Theory and Application," *In-Tech*, pp. 1–20, Aug. 2012.

[60] S. Singh, N. Kumar, and A. Monga, "To implement resistance measurement techniques using DC bridge circuits (Wheatstone and Kelvin double bridge) on National Instruments ELVIS-II workstation," *Int. J. Adv. Res. Comput. Eng. Technol.*, vol. 4, no. May, pp. 1686–1690, 2015.

APPENDICES

Appendix A: Derivation of Heater (*P(L)*%) Equation

In order to derive the equation for (*P(L)*%) of the carbon fiber heater, the electrodes and the carbon fiber sheet are treated as distributed resistors. We consider an infinitesimal slice of length δx where x is the position coordinate along the length of the electrodes (see Figure A-1). By Ohm's Law, the resistance of each electrode within each slice is:

$$\frac{\rho_{Ag}}{t_{Ag} \times W_{Ag}} \delta x = R_{Ag} \delta x$$

And the resistance of the carbon fiber within each slice is:

$$\frac{\rho_{CF} \times W_{CF}}{t_{CF}} \frac{1}{\delta x} = \frac{R_{CF}}{\delta x}$$

R_{Ag} is the resistance of the silver electrodes per unit length. R_{CF} is the resistance of the carbon fiber sheet per unit width.

The voltage across the carbon fiber sheet (V) and the current through the electrodes (I) are functions of position x along the electrodes as voltage is dropped across the electrodes. By considering the voltage and current changes across the infinitesimal section of the heater, one can derive the following differential equations:

$$V = 2IR_{Ag} \delta x - \frac{\delta I R_{CF}}{\delta x}$$

$V + \delta V = -\delta I \frac{R_{CF}}{\delta x}$

$\delta V = -2IR_{Ag}\delta x$

$\frac{\delta V}{\delta x} = -2IR_{Ag}$

$I = -\frac{1}{2R_{Ag}}\frac{\delta V}{\delta x} = -\frac{1}{2R_{Ag}}\frac{dV}{dx}$ (i)

$V \approx -\delta I \frac{R_{CF}}{\delta x} = -R_{CF}\frac{dI}{dx}$ (ii)

Combining (i) and (ii):

$I = \frac{R_{CF}}{2R_{Ag}}\frac{d^2I}{dx^2}$

Solving the differential equation:

$I(x) = I_1 e^{-\alpha x} + I_2 e^{\alpha x}$

$\alpha = \sqrt{\frac{2R_{Ag}}{R_{CF}}}$

Boundary condition: no current can flow beyond the end of the electrodes at x=L.

$I(L) = 0 = I_1 e^{-\alpha L} + I_2 e^{\alpha L}$

$I_1 = -I_2 e^{2\alpha L}$

From (ii):

$$V(x) = -R_{CF}\frac{dI}{dx} = -R_{CF}(-\alpha I_1 e^{-\alpha x} + \alpha I_2 e^{\alpha x})$$

Boundary condition: the applied voltage at x=0 is V_0.

$$V(x = 0) = V_0 = R_{CF}\alpha(I_1 - I_2)$$

Substitute I_1:

$$V_0 = R_{CF}\alpha(-I_2 e^{2\alpha L} - I_2)$$

$$I_2 = -\frac{V_0}{R_{CF}\alpha(1+e^{2\alpha L})}$$

$$I_1 = -I_2 e^{2\alpha L} = \frac{V_0 e^{2\alpha L}}{R_{CF}\alpha(1+e^{2\alpha L})}$$

$$V(x) = R_{CF}\alpha\left(\frac{V_0 e^{2\alpha L}}{R_{CF}\alpha(1+e^{2\alpha L})}e^{-\alpha x} + \frac{V_0}{R_{CF}\alpha(1+e^{2\alpha L})}e^{\alpha x}\right) = V_0\frac{e^{-\alpha x}e^{2\alpha L}+e^{\alpha x}}{1+e^{2\alpha L}}$$

The electrical power dissipated in the carbon fiber resistor in a segment of width δx is converted into heat as desired. This power can be calculated using the well-known formula for electrical power dissipated in a resistor V^2/R:

$$P_{CF}(x) = \frac{V(x)^2}{R_{CF}/\delta x}$$

Heat generation diminishes for larger x and is smallest for x=L. As a metric for the non-uniformity in heat generation across the heater, the heater (*P(L)*%) at x=L is calculated by dividing the electrical power dissipated in the carbon fiber at x=L by the same at x=0:

$$P(L)\% = \frac{P_{CF}(L)}{P_{CF}(0)} = \frac{V(L)^2 \times \frac{\delta x}{R_{CF}}}{V_0^2 \times \frac{\delta x}{R_{CF}}} = \frac{\left(V_0 \frac{e^{-\alpha L} e^{2\alpha L} + e^{\alpha L}}{1+e^{2\alpha L}}\right)^2}{V_0^2} = \frac{4e^{2\alpha L}}{(1+e^{2\alpha L})^2} =$$

$$\frac{\mathbf{4\,exp}\left(\mathbf{2}L\sqrt{\mathbf{2}R_{Ag}/R_{CF}}\right)}{\left(\mathbf{1}+\mathbf{exp}\left(\mathbf{2}L\sqrt{\mathbf{2}R_{Ag}/R_{CF}}\right)\right)^{\mathbf{2}}}$$

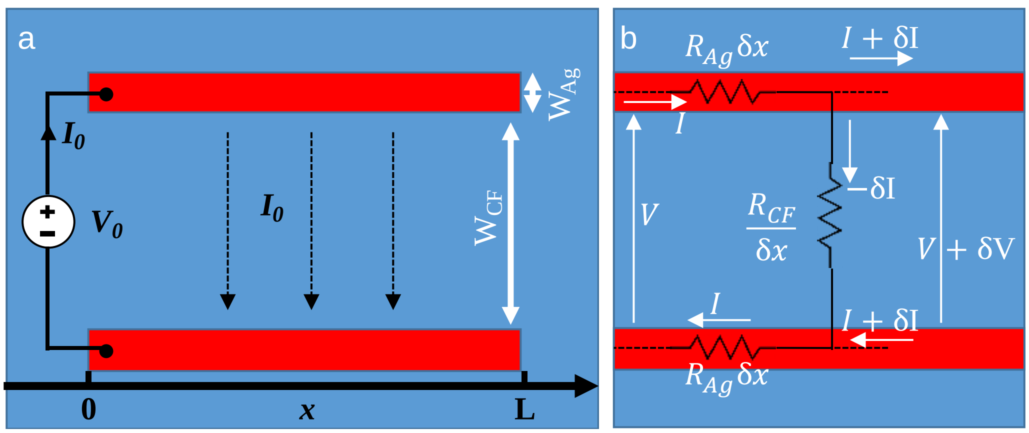

Figure A-1. (a) Geometry of the complete heater. The coordinate along the length of the electrodes is x. Current is injected at x=0. (b) Infinitesimal section of the heater with length δx. Voltage and current are functions of position x and increase by an infinitesimal amount δV and δI over the distance δx. The change in current δI is due to current division between the electrode and the carbon fiber. The change in voltage δV is due to the voltage drop across the electrodes.

Appendix B: Derivation of resistance in Kelvin Double Bridge circuit from measured voltage V_G

Figure B-1 shows the Kelvin double bridge circuit to determine the resistance of the carbon fiber sheet between the voltage measurement electrodes (R_x) by measuring the voltage (V_G). Here, the relationship between V_G and R_x is derived.

It is assumed that R_1, R_2, R_1', R_2' all have the same value. This means the voltage at their midpoint (V_{G1} and V_{G2} respectively) is half of the total voltage across the two resistors in series (potential divider).

It is further assumed that R_1, R_2, R_1', R_2' are sufficiently large compared to the other resistances in the circuit that the current through R_1, R_2, R_1', R_2' is negligible. Any parasitic resistance e.g. contact resistance in series with R_1, R_2, R_1', R_2' can be neglected.

With these assumptions, R_x can be calculated from V_G using Kirchoff's Current and Voltage Laws:

$$V_{G1} = I(R_3 + R_C/2)$$

$$V_{G2} = \frac{I(R_x+R_3+R_C)}{2}$$

$$V_G = V_{G2} - V_{G1} = \frac{I(R_x-R_3)}{2}$$

Instead of using a pre-determined value for R_3, the circuit is calibrated by measuring V_G when R_x is set to zero i.e. when a short circuit is measured instead of the actual device of interest.

$$R_3 = -\frac{2V_G|_{R_x=0}}{I}$$

$$R_x = \frac{2V_G}{I} + R_3 = \frac{2(V_G - V_G|_{R_x=0})}{I}$$

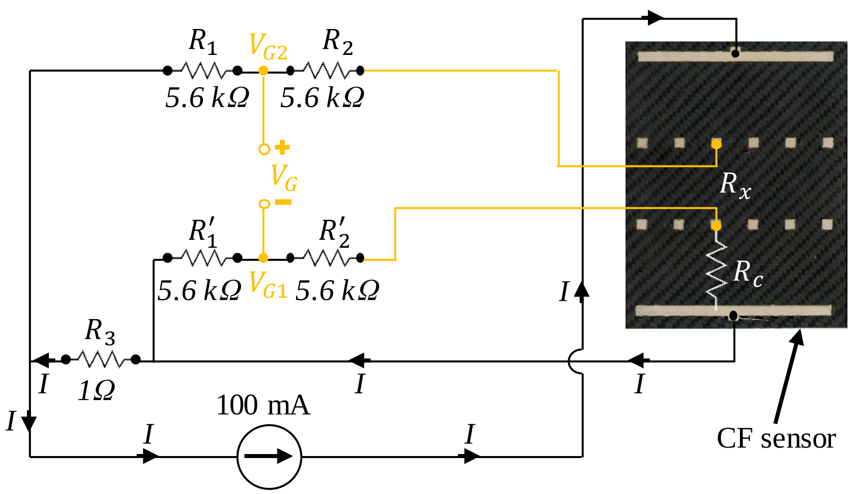

Figure B-1. Kelvin double bridge circuit combined with 4-point probing technique. R_x is the resistance of the carbon fiber sheet that is under test. V_G is the measured voltage.

Appendix C: Damage Sensor Simulation

The Sentaurus program uses three main scripts to conduct the simulation (SDE, SDEVICE and INSPECT). In the SDE command file the physical structure and dimensions of the device are defined as shown in the code (sde_dvs.cmd). All dimensions are in micrometer. In this code the material, shapes and locations of the features are defined. The mesh used to solve the finite element module is also defined in this script. The mesh size changes depending on the location in a range between 300 – 2000 μm as shown in Figure C-1. A mesh size larger than 2000 μm is considered too coarse and affects the accuracy of the results. In the location where the silver and silicon meet the mesh size is defined as 1 μm and increases by a rate of 0.5 away from the junction. This is because we want to create a finer mesh close to the contacts where we would see the most variation in parameters, but want to keep it coarse away from the contacts to save computational time and memory.

sde_dvs.cmd

```
(sdegeo:create-rectangle (position 0 0 0)  (position 125000 96000 0)
"Silicon" "region_1")
(sdedr:define-constant-profile "ConstantProfileDefinition_1"
"BoronActiveConcentration" 1e18)
(sdedr:define-constant-profile-region "ConstantProfilePlacement_1"
"ConstantProfileDefinition_1" "region_1")

(sdegeo:create-rectangle (position 115000 6000 0)  (position 119000
90000 0) "Silver" "GND")
```

```
(sdegeo:create-rectangle (position 6000 6000 0)  (position 10000 90000 0) "Silver" "Curr_1")

(sdegeo:insert-vertex (position 6000 46000 0))
(sdegeo:insert-vertex (position 6000 50000 0))

(sdegeo:insert-vertex (position 119000 46000 0))
(sdegeo:insert-vertex (position 119000 50000 0))

(sdegeo:define-contact-set "V1" 4  (color:rgb 0 0 1 ) "##")
(sdegeo:define-contact-set "V2" 4  (color:rgb 0 0 1 ) "##")

(sdegeo:define-2d-contact (list (car (find-edge-id (position 6000 48000 0)))) "V1")
(sdegeo:define-2d-contact (list (car (find-edge-id (position 119000 48000 0)))) "V2")

(sdegeo:create-rectangle (position 43000 6000 0)  (position 47000 10000 0) "Silver" "pad_1")
(sdegeo:create-rectangle (position 43000 22000 0)  (position 47000 26000 0) "Silver" "pad_2")
(sdegeo:create-rectangle (position 43000 38000 0)  (position 47000 42000 0) "Silver" "pad_3")
(sdegeo:create-rectangle (position 43000 54000 0)  (position 47000 58000 0) "Silver" "pad_4")
(sdegeo:create-rectangle (position 43000 70000 0)  (position 47000 74000 0) "Silver" "pad_5")
(sdegeo:create-rectangle (position 43000 86000 0)  (position 47000 90000 0) "Silver" "pad_6")

(sdegeo:create-rectangle (position 78000 6000 0)  (position 82000 10000 0) "Silver" "pad_7")
(sdegeo:create-rectangle (position 78000 22000 0)  (position 82000 26000 0) "Silver" "pad_8")
(sdegeo:create-rectangle (position 78000 38000 0)  (position 82000 42000 0) "Silver" "pad_9")
(sdegeo:create-rectangle (position 78000 54000 0)  (position 82000 58000 0) "Silver" "pad_10")
(sdegeo:create-rectangle (position 78000 70000 0)  (position 82000 74000 0) "Silver" "pad_11")
```

```
(sdegeo:create-rectangle (position 78000 86000 0)  (position 82000
90000 0) "Silver" "pad_12")

(sdegeo:create-rectangle (position 50000 @X@ 0)  (position 75000
@Y@ 0) "SiO2" "damage")

(sdedr:define-refeval-window "RefEvalWin_1" "Rectangle"  (position -
5126.799805 -5772.390625 0) (position 99520.765625 103374.484375
0))
(sdedr:define-refinement-size "RefinementDefinition_1" 2000 2000 300
300 )

(sdedr:define-refinement-placement "RefinementPlacement_1"
"RefinementDefinition_1" (list "window" "RefEvalWin_1" ) )

(sdedr:define-refinement-function "RefinementDefinition_1" "MaxLenInt"
"Silicon" "Silver" 1 0.5)

(sde:build-mesh "" "n@node@")
```

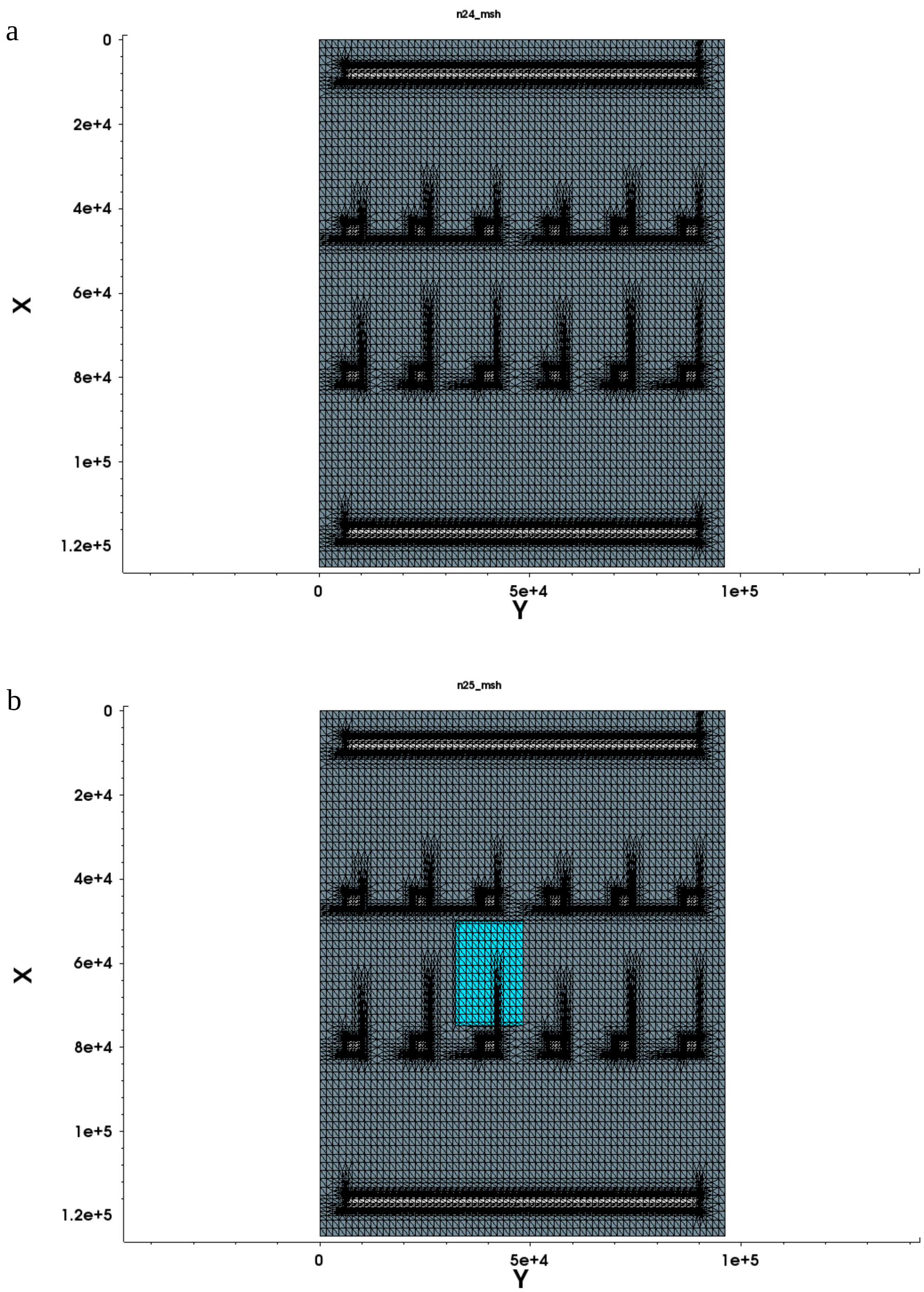

Figure C-1. Sentaurus simulation of 1D damage sensor showing the mesh size variation in different locations. a) Without damage; b) With damage in location 3

SDEVICE is the solving module that applies the physics models to calculate the behavior of the device. Two scripts are defined for this module. (sdevice.par) defines the variable parameters of the materials. In this case the work function of the silver material is defined. (sdevice_des.cmd) defines the physics and math models and equations used.

sdevice.par

```
#define ParFileDir .

Material="Silver" {
        Bandgap { WorkFunction = 5.1761 # [eV]}
  #includeext "ParFileDir/Silver.par"

}
```

sdevice_des.cmd

```
File {
  * Input Files

Grid      = "@tdr@"

* Output Files

Current = "n@node@"

  Plot    = "n@node@"

  Output  = "n@node@"
}

Electrode {
  { Name="V1"       Voltage=0 }
{ Name="V2"      Voltage=0 }
 }
```

```
Physics(MaterialInterface = "Silver/Silicon") { Schottky }

* Physics {
* Mobility( DopingDep HighFieldSat Enormal )

* EffectiveIntrinsicDensity( OldSlotboom )
*  Recombination( SRH (DopingDependence) Auger Avalanche )
* }


Plot {
  eDensity hDensity eCurrent hCurrent
  Potential SpaceCharge ElectricField
  eMobility hMobility eVelocity hVelocity
  Doping DonorConcentration AcceptorConcentration
}


Math {
*-- Parallelization on multi-CPU machine --*
  Number_Of_Threads=1   * change the number of threads to > 1 to make

* parallelization possible. First ensure your machine

* has shared-memory multi-CPU configuration.
*-- Numeric/Solver Controls --*
  Extrapolate
* switches on solution extrapolation along a bias ramp
  Derivatives
* considers mobility derivatives in Jacobian
  Iterations=8
* maximum-allowed number of Newton iterations (3D)
  RelErrControl
* switches on the relative error control for solution

* variables (on by default)
  Digits=5
* relative error control value. Iterations stop if

* dx/x < 10^(-Digits)
  Method=ILS
```

```
* use the iterative linear solver with default parameter
  NotDamped=100
* number of Newton iterations over which the RHS-norm

* is allowed to increase
  Transient=BE
* switches on BE transient method
}

Solve {
*- Buildup of initial solution:
   Coupled(Iterations=100){ Poisson }
   Coupled{ Poisson Electron Hole }
*- Bias L1

Quasistationary(

InitialStep=0.002 MinStep=0.00005 MaxStep=0.002

Goal{ Name="V1" Voltage=1 }

   )
{ Coupled{ Poisson Electron Hole } }

}
```

Finally, in INSPECT formulas for required calculations could be defined. In this case, as shown in code (inspect_ins.cmd), the resistance of the sheet is extracted and used to calculate the value of the electrical current.

sdevice_des.cmd

```
set ProjectName "IV_R"
set CurveName "IV(@node@)"

proj_load @plot@ $ProjectName

cv_createDS $CurveName "$ProjectName V1 OuterVoltage" "$ProjectName V1 TotalCurrent" y

set R [cv_compute "1/Rout(<$CurveName>)/1000" A A A A]

ft_scalar I [format %.2e $R]
```